IEEE Access
Multidisciplinary | Rapid Review | Open Access Journal

Received March 16, 2021, accepted April 5, 2021, date of publication April 8, 2021, date of current version April 16, 2021.

*Digital Object Identifier 10.1109/ACCESS.2021.3071760*

# Image Reconstruction Using Variable Exponential Function Regularization for Wide-Field Polarization Modulation Imaging

**QIONG WU[1], KUN GAO[1], MU LI[2], ZHENZHOU ZHANG[1], ZIZHENG HUA[1], HANWEN ZHAO[3], JICHUAN XIONG[3], ZEYANG DOU[1], HONG WANG[1], AND PEILIN YU[1]**

[1]Key Laboratory of Photoelectronic Imaging Technology and System, Ministry of Education, School of Optics and Photonics, Beijing Institute of Technology, Beijing 100081, China
[2]AI Platform of Meituan-Dianping Group, Beijing 100081, China
[3]School of Electronic and Optical Engineering, Nanjing University of Science and Technology, Nanjing 210094, China

Corresponding author: Kun Gao (gaokun@bit.edu.cn)

This work was supported in part by the Special Project of the Science and Technology Ministry of China under Grant 2017YFF0107102, in part by the National Natural Science Foundation of China under Grant 61875013 and Grant 61827814, and in part by the Beijing Natural Science Foundation under Grant Z19J00064.

**ABSTRACT** Polarization modulation imaging technology plays an important role in microscopic super-resolution imaging. However, the specimen medium contains retardancy, while charge-coupled devices may provide discrete under-sampling, and the coupled wavefronts consisting of the polarization state of the light and the anisotropic distribution of the specimen can lead to vectorial phase fitting degradation. Considering that the point spread function (PSF) of the main degradation parts can be regarded as an asymmetric generalized Gaussian distribution with uncertain parameters, an adaptive image reconstruction method is proposed based on variable exponential function regularization. The proposed method concentrates on the diversity of the PSF and uses a variable exponent regularization to improve flexibility of the kernel. Moreover, it can balance image edge preservation and provide staircase artifact suppression, which reduces the over- and under-reconstruction of the microscopic images effectively. By optimizing the Split–Bregman algorithm, we create an efficient method that minimizes the iterative loss function under the premise of achieving high estimation accuracy. Compared with other methods, the experimental results reveal better effectiveness and robustness of the proposed method, with improvements of 18% in the peak signal-to-noise ratio, 21% in the structural similarity index measurement, and 337% in the mean structural similarity index measurement.

**INDEX TERMS** Image reconstruction, variable exponential function regularization, optimized Split–Bregman, polarization imaging.

## I. INTRODUCTION

Super-resolution, wide-field imaging and spectroscopy are widely used to characterize subwavelength nanoparticles [1], [2]. Wide-field optical polarization modulation imaging modulates the parameters characterizing the vector state of the light wave, such as the polarization state, the direction of the wave vector, and the phase of the wave surface of the incident light. Then, the variation of the near-field parameters can be retrieved according to Maxwell equation from the obtained image sequence. Finally, a far-field super-resolution image that overcomes the diffraction limit can be retrieved and reconstructed.

Nevertheless, as degradation imposed by the experimental setup, it is impossible to obtain a perfectly sharp image of the specimen. The specimen medium contains retardancy [3], [4], and charge-coupled devices (CCDs) can lead to discrete under-sampling [5], [6], while the coupled wavefronts consisting of the polarization state of the light and the anisotropic distribution of the specimen can result in vectorial phase fitting degradation [7], [8]. Since the uncertain estimation of the degradation imaging system, it is very difficult to accurately determine the point-spread function (PSF). Indeed, accurate estimation of the PSF using sharp images is a premise for

The associate editor coordinating the review of this manuscript and approving it for publication was Wen Chen.

ensuring the quality of image reconstruction [9], [10]. In this work, we focus on the effect of the absence of prior information and degradation parameters on the reconstruction, and study various methods to balance image-detail enhancement and noise suppression.

Regularization is one of the most effective methods to overcome the limitations of image reconstruction [11]. To introduce additional constraints to ill-posed problems, the regularization model and the selected kernels are particularly important. Typical regularization models can be separated into two categories. The first consists of studies based on Total Variation (TV) regularization. For example, Daniele and Paolo [12] provided both analyses and experiments to get a clearer picture of blind deconvolution. Chen *et al.* [13] proposed a combinational regularization model for synthetic aperture radar image despeckling. Du *et al.* [14] proposed a joint weighted nuclear norm and TV regularization method to decrease the noise of the hyperspectral imaging data. The second category contains studies based on Tikhonov regularization. For example, Chen *et al.* [15] focused on a Tikhonov regularization method for inverse mixed variational inequalities. Zhai *et al.* [16] proposed a regularization matrix construction approach based on the minimum mean square error. Lu *et al.* [17] proposed a fusion method based on Tikhonov regularization and detailed reconstruction. All the studies mentioned here have demonstrated certain advantages in terms of accuracy, robustness, and/or compactness. However, these approaches also have some drawbacks. TV regularization smooths the wings of the PSF yet fails to keep the edges, while Tikhonov regularization strengthens PSF edges, it still forms a 'staircase artifacts' in the wings.

Recently, deep learning has also been widely used in degraded image reconstruction. Rivenson *et al.* [18] proposed a neural network to reconstruct the phase and amplitude images of various samples via a hologram. Xu *et al.* [19] developed a trilateral weighted sparse coding scheme for robust real-world image denoising. Yue *et al.* [20] proposed a novel unified framework to simultaneously deal with noise removal and generation. Cai and Wei [21] proposed a novel deep generative model equipped with a brand new style extractor which can extract style features from ground truth values. These networks were confirmed to be effective for image reconstruction. As the network required a large number of specimens as a training set, currently there is no public dataset of wide-field subwavelength nanoparticles that satisfies this requirement. Moreover, nanoparticle super-resolution reconstruction is more complicated than image reconstruction under natural light, which increases the computational complexity. As the parameters of the degradation model are unknown, the reconstruction method based on deep learning is worse than what can be achieved with conventional methods [19], [20]. Although inpainting can provide a good visualization effect on image reconstruction, it is not suitable for revealing the microscopic properties of nanoparticles.

An early study [22] considered the degradation using a degenerate Gaussian model in which the relevant parameters were unknown. In our previous work [23], we demonstrated that the model of [22] follows an asymmetric generalized Gaussian distribution (AGGD). Nevertheless, the parameters of the model cannot be explicitly ascertained, which are easily affected by minor changes in the imaging process and instrumentation. Thus, we cannot use a constraint with a certain norm, such as the L1 norm (TV regularization) and L2 norm (Tikhonov regularization). Indeed, on the one hand, wide-field polarization imaging systems are affected by out-of-focus specimens in the optical axis. Image quality is degraded by the superposition of the clear image presented by the in-focus specimen and the unclear interference image of the out-of-focus specimen. On the other hand, traditional image reconstruction methods are all performed under a certain PSF. However, in actual systems, image degradation caused by multiple factors makes the PSF variable. Except for the degradation of the PSF, the noise of microscopic polarization imaging is related to the statistical properties of photons, which can be described by a Poisson distribution. The interaction between Poisson noise and degradation models leads to image degeneration, which makes PSF estimation extremely complex. Improper reconstruction enhances the degeneration of the image, or causes halo and artifacts [24]–[26]. It can interfere with further observations of the microscopic details of the particle or limit the accuracy of the obtained measurements.

Moreover, regularization and deep learning are mainly aimed at Gaussian degradation model to realize image reconstruction, but often fail to fit the AGGD model accurately. Improper reconstruction can also lead to severe over-reconstruction and under-reconstruction [27], [28]. Over-reconstruction will oversharp the particle boundary and singularities formed by degradation, resulting in high variance and low deviation of optimization results. Under-reconstruction will excessively blur the particle boundary and the background, resulting in low variance and high deviation of the optimization results. The improper reconstruction of optical field retrieval [7], [8] appears serious distortion in the particle boundary region, such as halo and artifacts. Polarization parameters cannot be properly restored.

In this paper, we propose a novel method based on variable exponential function regularization [29] to appropriately reconstruct the optical field retrieval imaging. The main advantage of our method is that it can adaptively determine the norm according to the degradation model and the characteristics of the image. This allows for a more flexible and effect approach to PSF estimation and reconstruction, and can effectively restrain the shortcomings of TV regularization and Tikhonov regularization. The proposed method does not rely on the initial value and is suitable for the reconstruction of mixed degradation model. Under the condition that the degraded prior knowledge is known, our

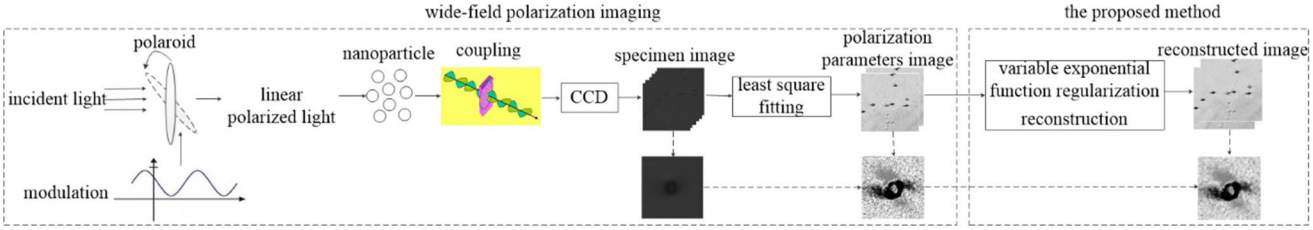


**FIGURE 1.** General outline of wide-field polarization imaging, and the processing methods adopted in the proposed method.

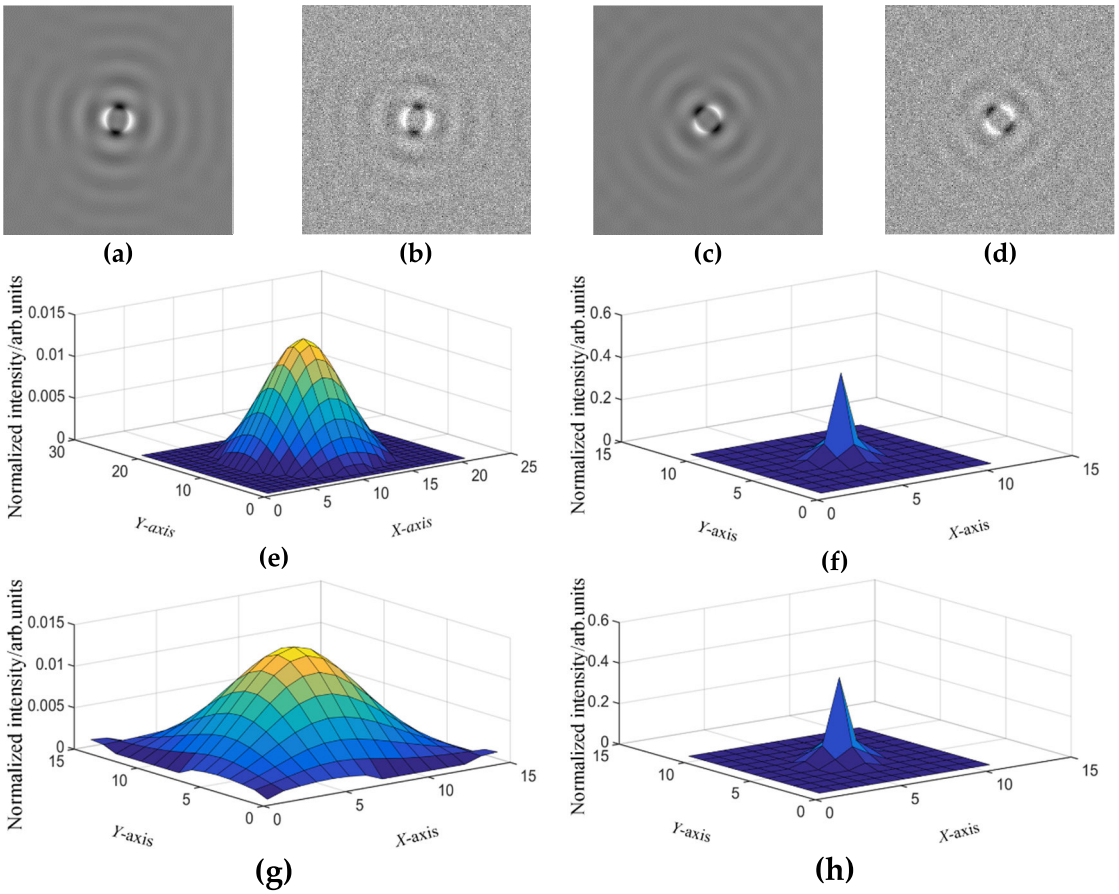


**FIGURE 2.** Image and the corresponding PSF degraded by the factors coupled with the polarized light and the anisotropic specimen medium. (a), (e) Original image and the corresponding PSF, (b), (f) degraded image and the corresponding PSF with AGGD degradative model, (c), (g) degraded image and the corresponding PSF with polarization angular errors, and (d), (h) degraded image and the corresponding PSF with AGGD degradative model and polarization angular errors.

previous research [29] has been validated in remote-sensing images. It demonstrates that the proposed method provides better support for image reconstruction, and efficaciously compensates for image degradation.

We have structured the remainder of the paper as follows. Section 2 presents an analysis of the degradation of wide-field polarization imaging and the design of our method. Section 3 analyses the simulated and experimental results of the proposed method compared with those obtained with other methods. Finally, the conclusions are provided in Section 4.

## II. MATERIALS AND METHODS

### A. DEGRADATION ANALYSIS OF WIDE-FIELD POLARIZATION IMAGING

As mentioned in Section 1, the PSF can be affected by multiple degradative factors in polarization imaging, thereby making it quite complex. Figure 1 depicts an outline of wide-field polarization imaging, and the processing approach used in the proposed method. Based on different amplitudes or wavefronts, the Stokes parameters can be retrieved using appropriate analyses for different sensors.

Let us first consider the noiseless case. Due to light transmission in the experimental setup, the air extinction, thermal lens radiation, and blackbody radiation all impact and degrade the polarized light wavefront. Similarly, the impurity and retardation properties of the specimen deteriorate the wavefront of the anisotropic specimen medium. Since the distribution and corresponding parameters of the variations are unknown, it directly results in uncertainties of the degradation model's parameters.

Figure 2 shows the image and the corresponding PSF generated by the finite-difference time-domain (FDTD) method degraded by the degradative factors mentioned above. Fig. 2(a) presents the original image, while Fig. 2(b) is a blurred image with AGGD model, where the shape parameter is 3.37 and the values of the left and right variances are 38.87 and 68.94, respectively. Fig. 2(c) shows a blurred image with an angular error of 90 degrees. Fig. 2(d) depicts a blurred image with AGGD model and angular errors, the parameters of which are the same as in Figs. 2(b) and 2(c), respectively. As can be seen in the figures, the image quality and PSFs have deteriorated to some extent.

Due to the rotation errors and static errors of the polarizer, the Stokes parameters have associated errors. The problem becomes more complicated when the AGGD degradation with uncertain parameters and Poisson noise are considered. Our current study attempts to maintain a balance between noise suppression and detailed retention during image reconstruction. To optimize the parameter estimation process, we use a regularization kernel to constrain the ill-posed problem in the appropriate solution space. We also propose the use of the variable exponential function regularization method, which is combined with the advantages of TV regularization and Tikhonov regularization to precisely estimate the PSF. The process allows us to implement self-adaptable parameter estimation and PSF estimation. It can balance coefficient sparsity and edge preservation, and further improve the quality of image reconstruction.

### B. MATHEMATICAL NOTATIONS AND MATRIX DIMENSION

The mathematical notations and their meanings used in this paper are shown in Table 1. Unless otherwise specified, the matrix dimensions presented in this paper are all $n \times n$ where $n = 1000$, and the initial value is zero matrix.

### C. LIGHT FIELD RETRIEVAL OF POLARIZATION MODULATION IMAGING

Since the incident light of the experimental setup is perpendicularly incident into the specimen, the light intensity perceived by CCD can be read as follow

$$I = \frac{I_0}{2}\left[1 + \sin 2\left(\frac{\pi}{2} - \rho\right)\sin\delta\right]. \tag{1}$$

Then, the Stokes parameters are retrieved by a mutual relationship between Jones and Muller model which are given as follow [7]

$$\begin{aligned} S_0 &= I_{dp}(1 + \sin\delta) \\ S_1 &= I_{dp}(1 + \sin\delta)\cos 2\rho \\ S_2 &= 2\sqrt{I_{dp}}(1 + \sin\delta)\cos 2\rho \\ S_3 &= 2\sqrt{I_{dp}}(1 + \sin\delta)\sin 2\rho. \end{aligned} \tag{2}$$

**TABLE 1. Mathematical notations.**

| Symbol | Quantity |
|---|---|
| $I_0$ | Unpolarized light intensity |
| $\rho$ | Incident polarization angle |
| $\delta$ | Polarization phase difference |
| $I_{dp}$ | Mean of the intensity of the incident light with different polarization angles and polarization phase differences |
| $x$ | Serious of stochastic variables |
| $\mu_{AGGD}$ | AGGD mean |
| $s_{AGGD}$ | Shape of the AGGD |
| $\sigma_l$ | Variances on the left side of the AGGD |
| $\sigma_r$ | Variances on the right side of the AGGD |
| $S$ | Skewness of the AGGD |
| $G(\bullet), \Phi(\bullet)$ | Convex function |
| $\mathbf{A}: \mathbb{R}^N \to \mathbb{R}^M$ | Linear operator |
| $\mathbf{u}, \mathbf{v}$ | Vector of dimension $n$ |
| $\mathbf{b}$ | Vector of dimension $m$ |
| $\mu, \varepsilon$ | Positive constants |
| $\mathbf{p} \in \partial G(\mathbf{x})$ | Subgradient of $G(\bullet)$ at $\mathbf{v}$ |
| $\mathbf{D}$ | Degraded image |
| $\mathbf{K}$ | Degraded PSF |
| $\mathbf{U}$ | Unknown precise image |
| $\mathbf{E}$ | Additive noise |
| $\mathbf{T}$ | Undimmed real PSF |
| $\mathbf{H}$ | Block circulant matrix with a circulant block formed by circularly transforming the column of $\mathbf{K}$, $\mathbf{K} \geq 0, \int_D \mathbf{K} d\sigma = 1$ |
| $D$ | Support domain of the PSF |
| $\mathbf{h}_x, \mathbf{h}_y$ | First-order finite differences in the horizontal and vertical directions of $\mathbf{H}$ |
| $n$ | Threshold which controls the decline rate of $p(m)$ |
| $m$ | Distinguishes marginal areas from the wings in $p(m)$ |
| $\alpha_1, \alpha_2, \alpha_3$ | Positive constants |
| $\mathbf{u}_x, \mathbf{u}_y$ | First-order finite differences in the horizontal and vertical directions of $\mathbf{U}$ |
| $\beta_1, \beta_2$ | Positive constants |
| $i$ | Number of iteration steps |
| $\mathbf{U}^{(i)}$ | Block circulant matrix with a circulant block generated by $\mathbf{U}$ |
| T | Conjugate |
| $\Delta$ | Laplacian operator |
| div | Divergence |

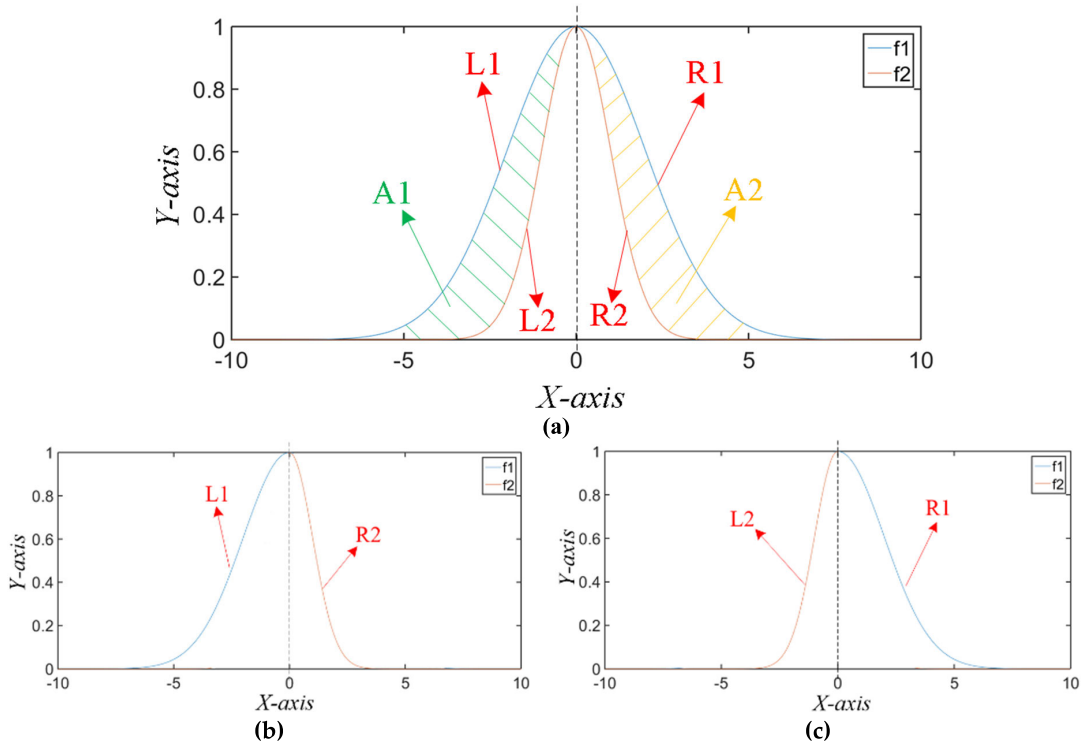


**FIGURE 3.** (a) Two Gaussian distribution functions, f1 and f2, and their over-reconstruction and under-reconstruction. (b) Right-skewed AGGD composed of L1 and R2, and (c) left-skewed AGGD composed of L2 and R1. The AGGD degradative model can be composed by L1 and R2, or L2 and R1, where the variances of left and right sides must not be the same.

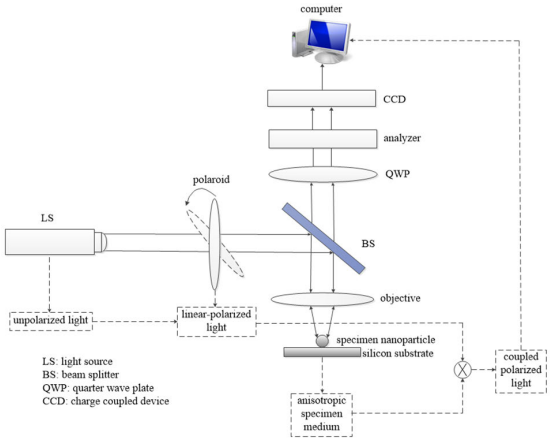


**FIGURE 4.** Experimental setup of the wide-field polarization modulation imaging system.

Due to the influence of AGGD degradation model, the polarization angle and polarization phase difference have errors. The proposed method compensates the degradation model by optimizing the PSF of the image. This optimizes the polarization parameters and conduces to obtain accurate light field information.

The polarization parameter imaging of the polarization modulation imaging retrieval used in this paper refers to the images of polarization angle and polarization phase difference. The polarization parameters range from 0 to $2\pi$. Polarization parameter imaging can be calculated by Stokes parameters.

### D. AGGD MODEL

An AGGD degradative model can be given by (3), as shown at the bottom of the next page.

$\Gamma(a)$ is a Gamma function which is defined as $\Gamma(a) = \int_0^\infty t^{a-1}e^{-t}dt, a > 0$.

The parameters $s_{AGGD}$, $\sigma_l$ and $\sigma_r$ are defined as follows

$$\begin{aligned} s_{AGGD} &= \rho^{-1}(R) \\ \sigma_l &= \delta_l\sqrt{\frac{\Gamma(3/\alpha)}{\Gamma(1/\alpha)}}, \\ \delta_l &= \sqrt{\frac{1}{N_l-1}\sum_{k=1,x_k<\mu_{AGGD}}^{N_l} x_k^2} \\ \sigma_r &= \delta_r\sqrt{\frac{\Gamma(3/\alpha)}{\Gamma(1/\alpha)}}, \\ \delta_r &= \sqrt{\frac{1}{N_r-1}\sum_{k=1,x_k\geq\mu_{AGGD}}^{N_r} x_k^2}, \end{aligned} \tag{4}$$

where

$$R = r\frac{(r^3+1)(r+1)}{(r^2+1)^2}, \quad r = \frac{\delta_l}{\delta_r}.$$

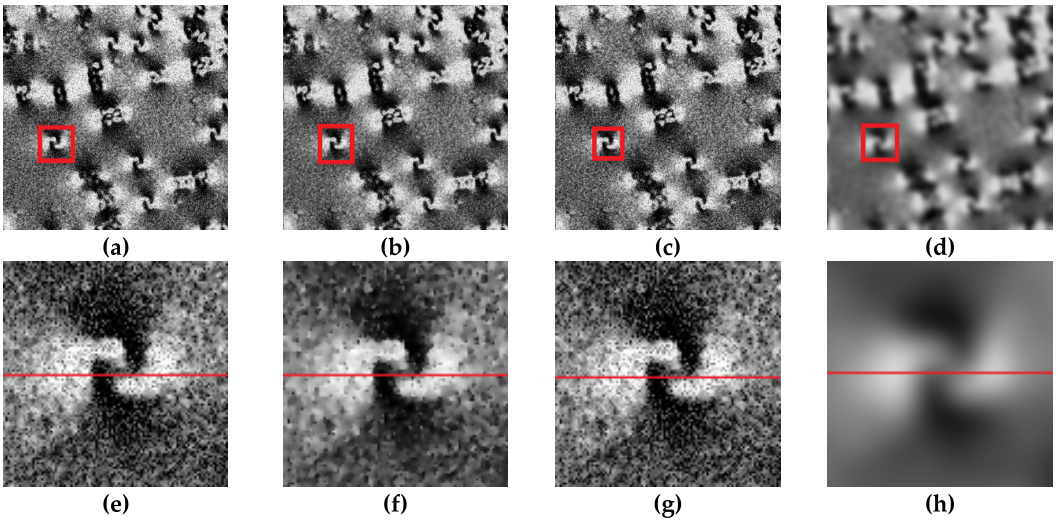


**FIGURE 5.** Comparison of the proposed method and the over- and under-reconstruction. (a), (e) original and zoomed-in images, (b), (f) image obtained with the proposed method and zoomed-in images, (c), (g) image obtained with over-reconstruction and zoomed-in images, and (d), (h) image obtained with under-reconstruction and zoomed-in images, where the red box represents the same position of (e), (f), (g), and (h).

As $\sigma_l \neq \sigma_r$ in the degradation model of the PSF, the skewness can be given by

$$S = \left(\sigma_r^4 - \sigma_l^4\right) \Gamma\left(4/s_{AGGD}\right) \sqrt{\frac{\left(\sigma_r + \sigma_l\right) \Gamma\left(1/s_{AGGD}\right)}{\left(\sigma_r^3 + \sigma_l^3\right)^3 \Gamma\left(3/s_{AGGD}\right)^3}}. \tag{5}$$

If $S < 0$, the data are right-skewed, otherwise they are left-skewed.

Generally, TV regularization, Tikhonov regularization, inverse filtering, and Wiener filtering are effective on Gaussian model. As AGGD has asymmetry on the left and right sides, it can result in severe over- or under-reconstruction. Fig. 3(a) shows two Gaussian distributions and their over-reconstruction and under-reconstruction, where $f1 \sim N(0, 2)$ and $f2 \sim N(0, 1)$. L1 and R1 are the left and right side of f1, and L2 and R2 are the left and right side of f2. A1 is the difference between L1 and L2, and A2 is the difference between R1 and R2.

Assume the AGGD is composed of L1 and R2, as shown in Fig. 3(b), and the fitting curve is f1. The fitting curve can fit L1 well, but it has serious over-reconstruction when using R1 to fit R2. Similarly, when f2 is used as the fitting curve, under-reconstruction occurs when L1 is fitted. The same situation is presented in Fig. 3(c). Thus, it is impossible to fit the AGGD with a symmetric structure as done in these conventional methods. As the PSF obtained after reasonable reconstruction is important in image reconstruction or analysis [7], we propose the use of variable exponential function regularization.

### *E. SPLIT–BREGMAN ALGORITHM*

Assume $G(\cdot)$ is a convex function. Let us first consider the unconstrained optimization problem

$$\min G(\mathbf{u}) + \frac{1}{2\mu} \|\mathbf{A}\mathbf{u} - \mathbf{b}\|_2^2. \tag{6}$$

When $m$ is much less than $n$, it is difficult to solve the above problem.

To solve this problem, we first introduce the Bregman distance. The Bregman distance between $\mathbf{u}$ and $\mathbf{v}$ is defined as follows

$$D_G^{\mathbf{p}}(\mathbf{u}, \mathbf{v}) = G(\mathbf{u}) - G(\mathbf{v}) - \langle \mathbf{p}, \mathbf{u} - \mathbf{v} \rangle, \tag{7}$$

where $D_G^{\mathbf{p}}(\mathbf{u}, \mathbf{v}) \geq 0$. For any point $\mathbf{w}$ on the line connecting $\mathbf{u}$ and $\mathbf{v}$, $D_G^{\mathbf{p}}(\mathbf{u}, \mathbf{v}) \geq D_G^{\mathbf{p}}(\mathbf{w}, \mathbf{v})$. Assuming that $\mathbf{u}$ is the optimal solution and $\mathbf{v}$ is the iterative solution, $D_G^{\mathbf{p}}(\mathbf{u}, \mathbf{v})$ can be used to describe whether the iterative solution is or is not infinitely close to the optimal solution.

Now, let us go back to image reconstruction. The loss function can be given by

$$\min_{\mathbf{u},\mathbf{d}} |\mathbf{d}| + G(\mathbf{u}), \quad s.t.\ \mathbf{d} = \Phi(\mathbf{u}). \tag{8}$$

$$f_{AGGD} = \begin{cases} \dfrac{s_{AGGD}}{\left(\sigma_l + \sigma_r\right) \Gamma\left(1/s_{AGGD}\right)} \exp - \left(\dfrac{-(x - \mu_{AGGD})}{\sigma_l}\right)^{\alpha}, & x < \mu_{AGGD} \\ \dfrac{s_{AGGD}}{\left(\sigma_l + \sigma_r\right) \Gamma\left(1/s_{AGGD}\right)} \exp - \left(\dfrac{-(x - \mu_{AGGD})}{\sigma_r}\right)^{\alpha}, & x \geq \mu_{AGGD}, \end{cases} \tag{3}$$

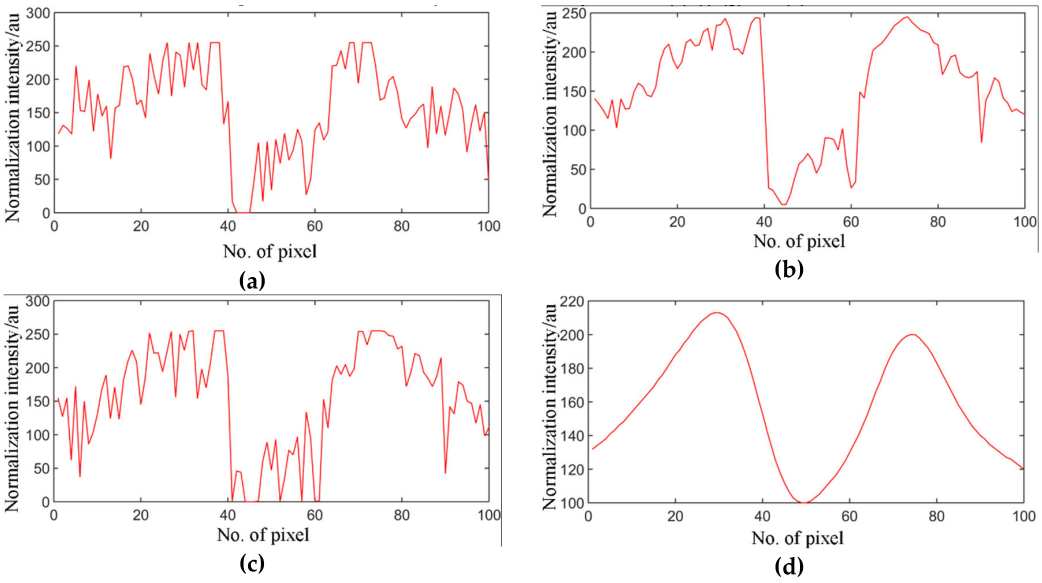


**FIGURE 6.** The light intensity profile of the particle along the tangent direction corresponding to Figs. 5(e-h). (a) light intensity change of all pixel points of origin image; (b) light intensity change of all pixel points of the reconstruction result of the proposed method; (c) light intensity change of particle pixel points of the reconstruction result of over-reconstruction; (d) light intensity change of particle pixel points of the reconstruction result of under-reconstruction.

We can transform (8) into an unconstrained optimization problem as follows

$$\min_{u,\mathbf{d}} |d| + G(\mathbf{u}) + \frac{\mu}{2} \|d - \Phi(\mathbf{u})\|_2^2, \tag{9}$$

Let $F_1(\mathbf{u}, \mathbf{d}) = |\mathbf{d}| + G(\mathbf{u})$ and $F_2(\mathbf{u}, \mathbf{d}) = \mathbf{d} - \Phi(\mathbf{u})$. Then, the iteration can be written as

$$\begin{aligned}
\left(\mathbf{u}^{k+1}, \mathbf{d}^{k+1}\right) &= \min_{\mathbf{u},\mathbf{d}} D_G^{\mathbf{p}}\left(\mathbf{u}, \mathbf{u}^k, \mathbf{d}, \mathbf{d}^k\right) \\
&\quad + \cdots + \frac{\mu}{2} \|d - \Phi(\mathbf{u})\|_2^2 \\
&= \min_{\mathbf{u},\mathbf{d}} F_1(\mathbf{u}, \mathbf{d}) - \left\langle \mathbf{p}_{\mathbf{u}}^k, \mathbf{u} - \mathbf{u}^k \right\rangle \\
&\quad - \cdots - \left\langle \mathbf{p}_{\mathbf{d}}^k, \mathbf{d} - \mathbf{d}^k \right\rangle + \frac{\mu}{2} \|F_2(\mathbf{u}, \mathbf{d})\|_2^2 \\
\mathbf{p}_{\mathbf{u}}^{k+1} &= \mathbf{p}_{\mathbf{d}}^k - \mu (\nabla\Phi)^T \left(\Phi\mathbf{u}^{k+1} - \mathbf{d}^{k+1}\right) \\
\mathbf{p}_{\mathbf{d}}^{k+1} &= \mathbf{p}_{\mathbf{d}}^k - \mu \left(\mathbf{d}^{k+1} - \Phi\mathbf{u}^{k+1}\right),
\end{aligned} \tag{10}$$

When $D_G^{\mathbf{p}}\left(\mathbf{u}^k, \mathbf{u}^{k-1}\right) \leq \varepsilon$, the iteration comes to an end, where $\varepsilon$ is a positive constant.

### F. VARIABLE EXPONENTIAL FUNCTION REGULARIZATION

Based on the theory of linear systems, the degenerative model of an optical system can be described as follows

$$\mathbf{D} = \mathbf{K} * \mathbf{U} + \mathbf{E}. \tag{11}$$

Estimating the PSF of a degraded image is a classical ill-posed problem.

To properly consider the complexity of the PSF, we propose a variable exponential function regularization kernel to ensure the existence of solutions, which can be defined as follows

$$R(\mathbf{H}) = \int |\nabla\mathbf{H}|^{p(|\nabla\mathbf{T}|)} \mathrm{d}\sigma, \tag{12}$$

where $\nabla\mathbf{H} = \left(\mathbf{h}_x, \mathbf{h}_y\right)$.

The adaptive optimization index of the estimated PSF is defined as follows

$$p(m) = 1 + \frac{1}{1 + nm^2}. \tag{13}$$

When $n$ is large, the regularization mode is mainly TV regularization. Similarly, when $n$ is small, Tikhonov regularization plays a leading role. Comparably, when in marginal areas, $m$ is large, the value of $p(m)$ tends to 1. Meanwhile, in wings where $m$ is small, $p(m)$ tends to 2. The proposed method can adaptively reconstruct an image by controlling $p(m)$. For wide-field polarization imaging, the proposed method strengthens the particle boundaries via Tikhonov regularization, and smooths the region via TV regularization.

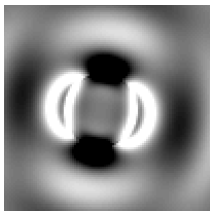

**FIGURE 7.** Original image with a polarizer angle of 0 degrees generated by the FDTD simulation without errors.

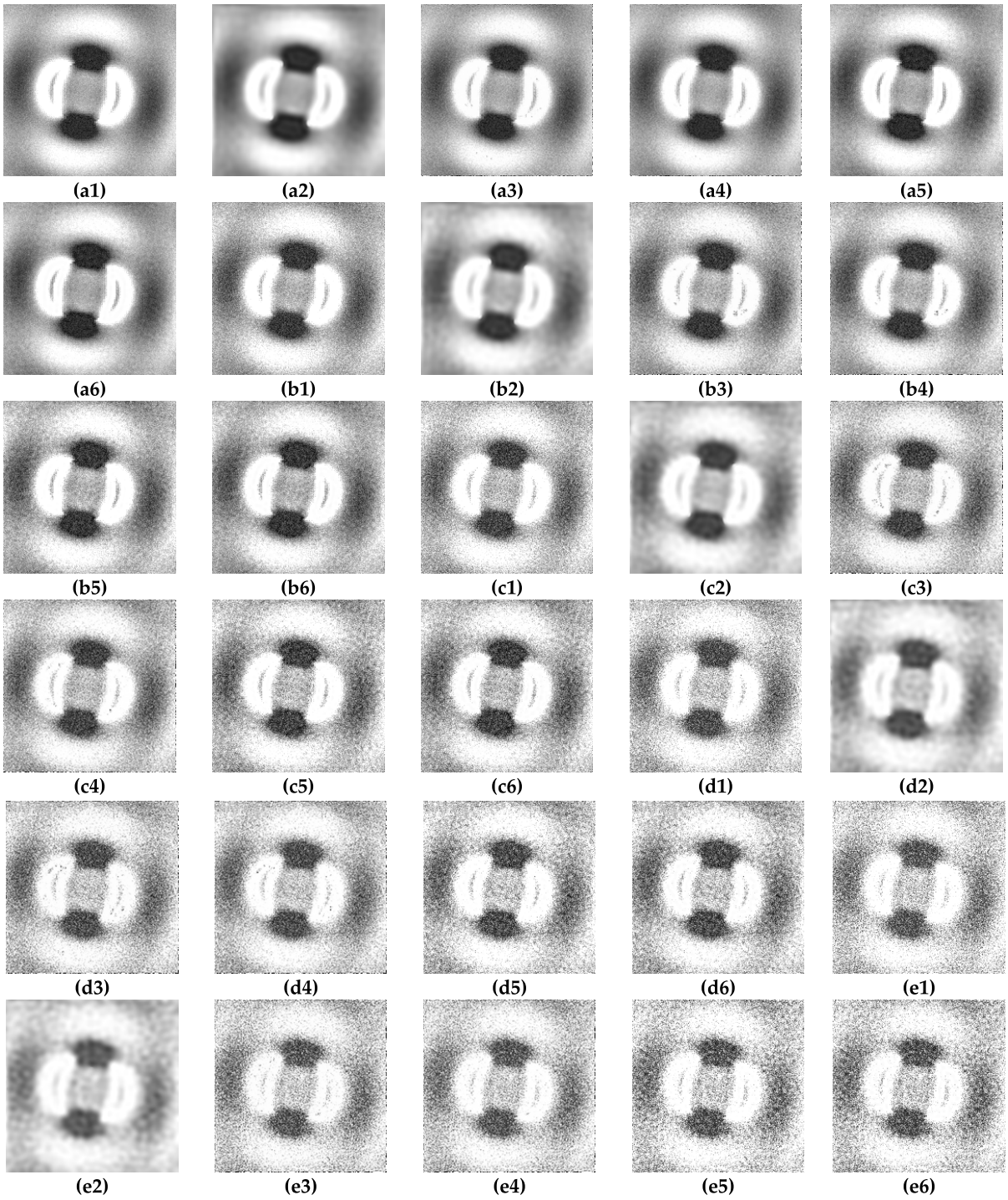


**FIGURE 8.** Comparison of the reconstructed results of the degraded image from the proposed method, Perrone's TV regularization, Lu's Tikhonov regularization, inverse filtering and Wiener filtering. Reconstructed results of the degraded image with mixed AGGD degradation with different parameters are shown in (a1–a6) where the shape parameter is 10 and the left and right variances are 3.21 and 38.4; (b1–b6) where the shape parameter is 10 and the left and right variances are 10.96 and 43.02; (c1–c6) where the shape parameter is 10 and the left and right variances are 19.76 and 50.59; (d1–d6) where the shape parameter is 5.62 and the left and right variances are 29.28 and 59.47; and (e1–e6) where the shape parameter is 3.36 and the left and right variances are 38.89 and 69.01. The parameter of additive Poisson noise is 10, 20, 30, 40, and 50 in panels (a1, b1, c1, d1, and e1), respectively. Next, (a1, b1, c1, d1, and e1) show the degraded image without processing, and the reconstructed results obtained with (a2, b2, c2, d2, and e2) the proposed method, (a3, b3, c3, d3, and e3) Perrone's TV regularization, (a4, b4, c4, d4, and e4) Lu's Tikhonov regularization, (a5, b5, c5, d5, and e5) inverse filtering, and (a6, b6, c6, d6, and e6) Wiener filtering.

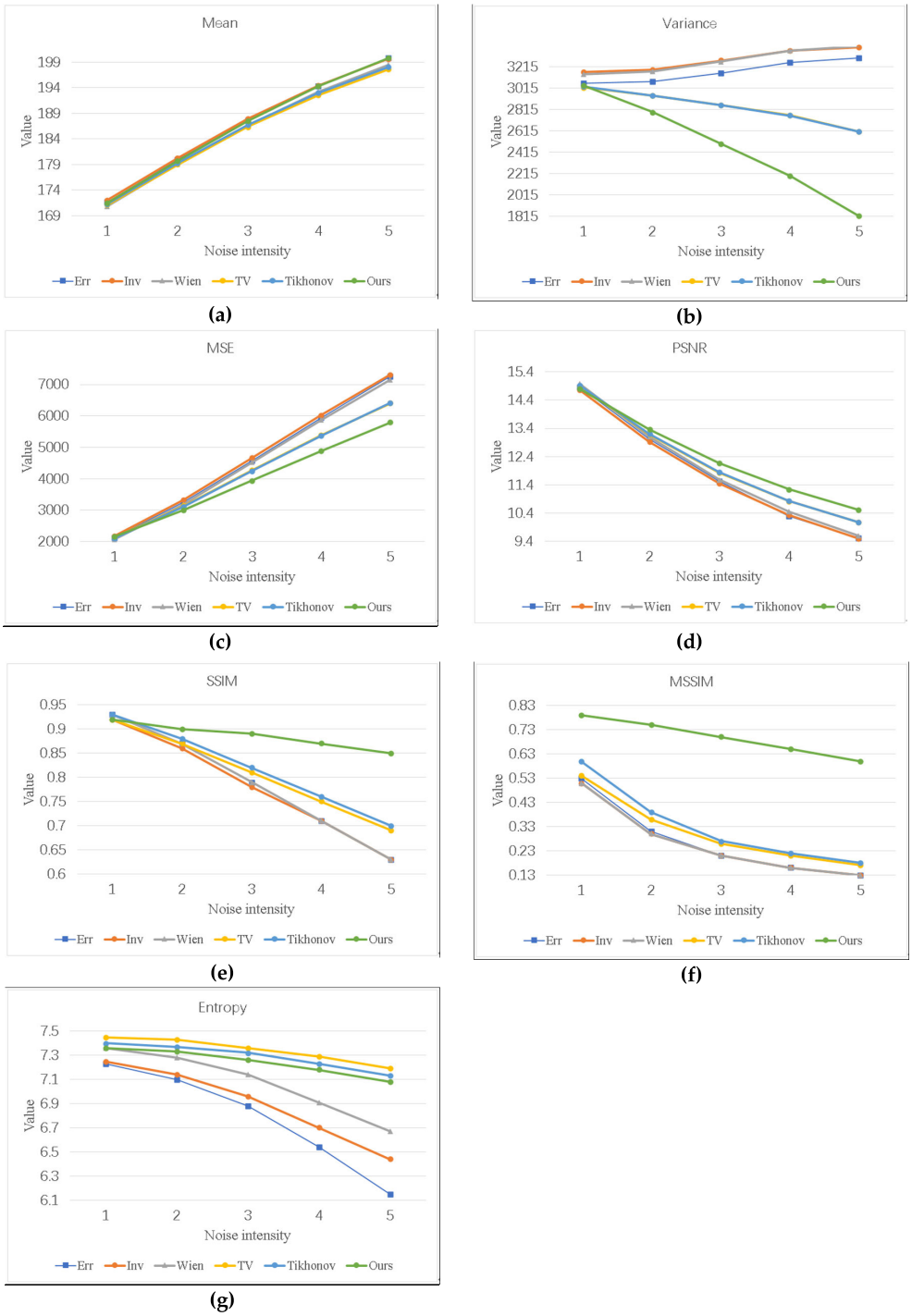


**FIGURE 9.** Objective assessment values of the images analyzed in Fig. 6. (a) Mean, (b) variance, (c) MSE, (d) PSNR, (e) SSIM, (f) MSSIM, and (g) entropy. The indices 1–5 of the $x$ -coordinate represent the corresponding images in Figs. 6 (a–e), respectively.

The loss function $J(\mathbf{H}, \mathbf{U})$ can be given by

$$\min_{\mathbf{H},\mathbf{U}} J(\mathbf{H}, \mathbf{U}) = \min_{\mathbf{H},\mathbf{U}} \left[ \alpha_3 \|\mathbf{H} \times \mathbf{U} - \mathbf{D}\|_2^2 + \alpha_1 R(\mathbf{H}) + \alpha_2 \int |\nabla \mathbf{U}| \, d\sigma \right], \tag{14}$$

where $\mathbf{U} \geq 0$. The previous work of our research group [29] demonstrated the existence and convergence of the solution to this loss function. Since the loss function of the proposed method is convex, it approximates the optimal solution point by point from the top according to the strong duality [30], and the optimal duality distance is zero.

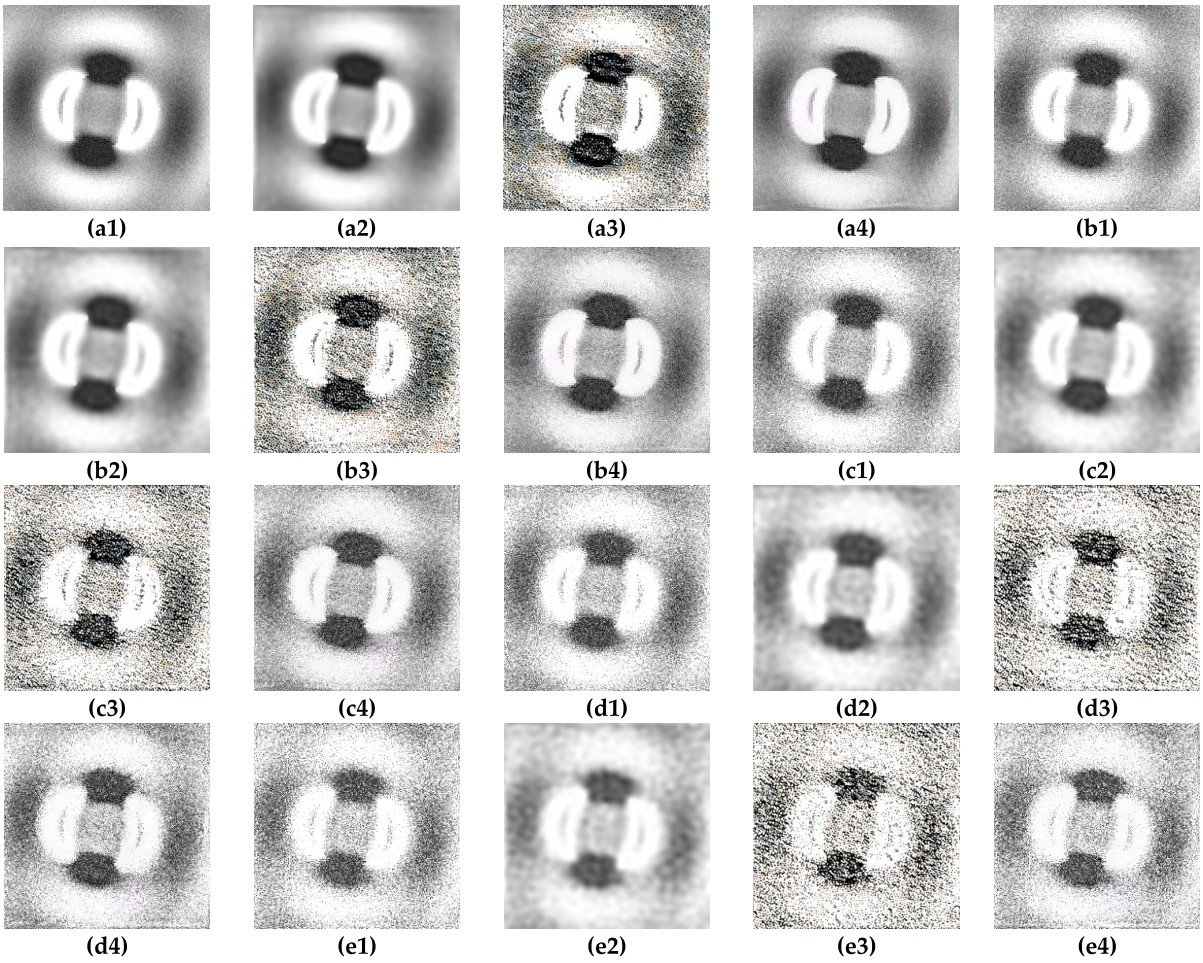


**FIGURE 10.** Comparison of the reconstructed results of the degraded image obtained with the proposed method, DPPSR, and DeblurGAN-v2. Reconstructed results of the degraded image with mixed AGGD degradation with different parameters are shown in (a1–a4), where the shape parameter is 10 and the left and right variances are 3.21 and 38.4; (b1–b4) where the shape parameter is 10 and the left and right variances are 10.96 and 43.02; (c1–c4) where the shape parameter is 10 and the left and right variances are 19.76 and 50.59; (d1–d4) where the shape parameter is 5.62 and the left and right variances are 29.28 and 59.47; and (e1–e4) where the shape parameter is 3.36 and the left and right variances are 38.89 and 69.01. The parameter of additive Poisson noise is 10, 20, 30, 40, and 50 in panels (a1, b1, c1, d1, and e1), respectively. Next, (a1, b1, c1, d1, and e1) show the degraded image without processing, and the reconstructed results obtained with (a2, b2, c2, d2, and e2) the proposed method, (a3, b3, c3, d3, and e3) DPPSR, and (a4, b4, c4, d4, and e4) DeblurGAN-v2.

We can get an optimal solution in closed sets, and selection of the initial values is robust.

Note that an L2 norm exists in $J(\mathbf{H}, \mathbf{U})$, which means that this problem can be regarded as convex optimization. To obtain a solution to (14), the Split–Bregman algorithm [31], [32] is used to optimize the loss function. Equation (14) can be transformed as follows

$$\min_{\mathbf{H},\mathbf{U}} J(\mathbf{H}, \mathbf{U}) = \min_{\mathbf{H},\mathbf{U}} \begin{bmatrix} \alpha_3 \|\mathbf{HU} - \mathbf{D}\|_2^2 + \alpha_1 \sum |\mathbf{a}_1|^{p(|\nabla \mathbf{T}|)} \\ + \cdots + \alpha_2 \sum |\mathbf{a}_2| + \beta_1 \|\mathbf{a}_1 - \nabla \mathbf{H}\|_2^2 \\ + \cdots + \beta_2 \|\mathbf{a}_2 - \nabla \mathbf{U}\|_2^2 \end{bmatrix}, \quad (15)$$

where $\mathbf{a}_1 = \nabla \mathbf{H}, \mathbf{a}_2 = \nabla \mathbf{U}, |\mathbf{a}| = \sqrt{\mathbf{a}_1^2 + \mathbf{a}_2^2}, \nabla \mathbf{U} = (\mathbf{u}_x, \mathbf{u}_y)$.

According to the Split–Bregman algorithm, the optimization iteration mode of (15) is given by

$$\left(\mathbf{H}^{(i+1)}, \mathbf{U}^{(i+1)}, \mathbf{a}_1^{(i+1)}, \mathbf{a}_2^{(i+1)}\right) = \arg\min_{\mathbf{H},\mathbf{U},\mathbf{a}_1,\mathbf{a}_2} \begin{bmatrix} \alpha_3 \|\mathbf{HU} - \mathbf{D}\|_2^2 + \alpha_1 \sum |\mathbf{a}_1|^{p(|\nabla \mathbf{T}|)} \\ + \ldots + \alpha_2 \sum |\mathbf{a}_2| + \beta_1 \left\|\mathbf{a}_1 - \nabla \mathbf{H} - \mathbf{s}_1^{(i)}\right\|_2^2 \\ + \ldots + \beta_2 \left\|\mathbf{a}_2 - \nabla \mathbf{U} - \mathbf{s}_2^{(i)}\right\|_2^2 \end{bmatrix}, \quad (16)$$

where $\mathbf{s}_1^{(i+1)} = \mathbf{s}_1^{(i)} + \nabla \mathbf{H}^{(i+1)} - \mathbf{a}_1^{(i+1)}, \mathbf{s}_2^{(i+1)} = \mathbf{s}_2^{(i)} + \nabla \mathbf{U}^{(i+1)} - \mathbf{a}_2^{(i+1)}$, and $i$ is the number of iteration steps.

Next, let us first fix $\mathbf{a_1}, \mathbf{s_1}$, and $\mathbf{U}$, for the subproblem of $\mathbf{H}$, which we can obtain via the variational principle

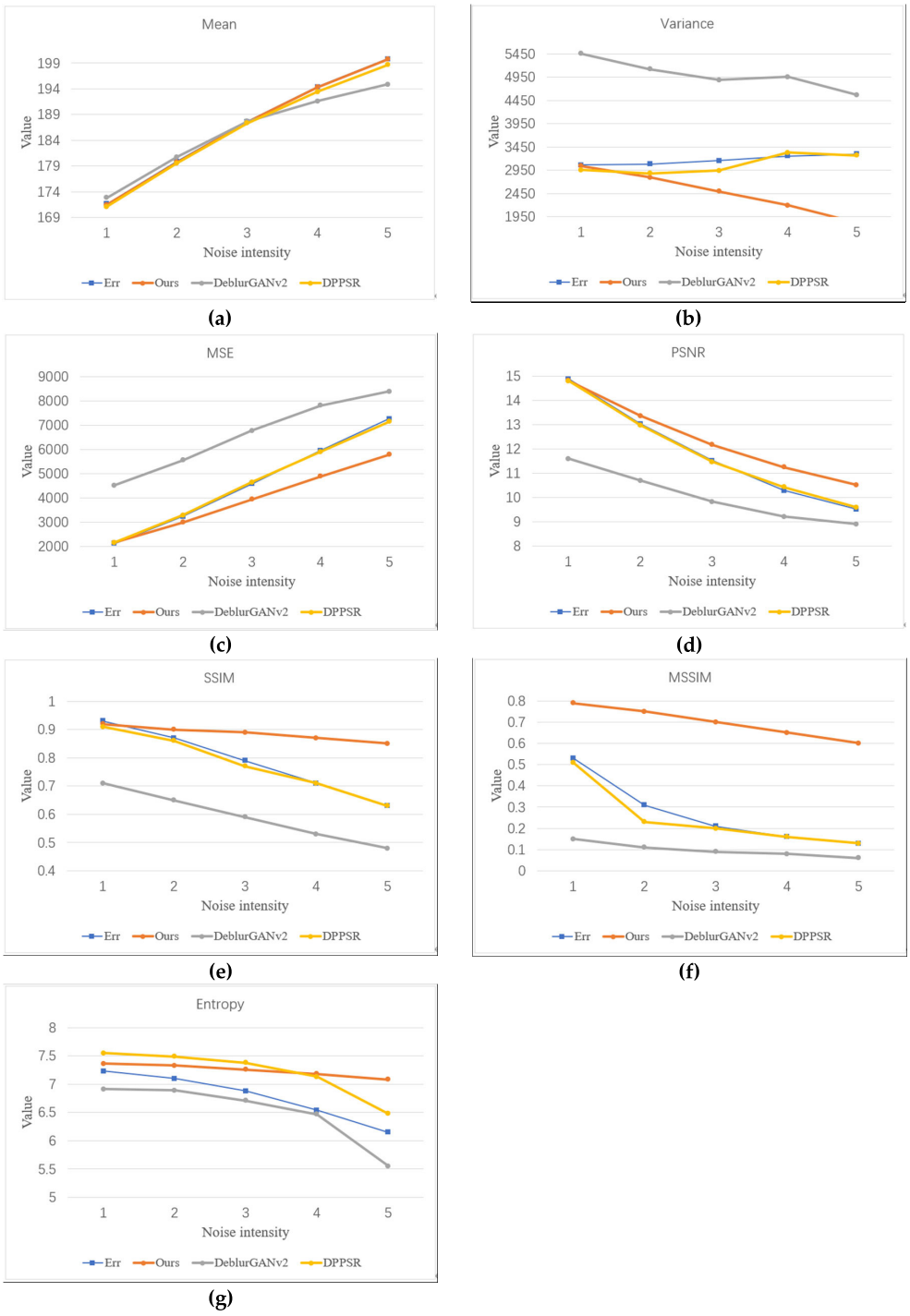


**FIGURE 11.** Objective assessment values of the images analyzed in Fig. 9. (a) Mean, (b) variance, (c) MSE, (d) PSNR, (e) SSIM, (f) MSSIM, and (g) entropy. The indices 1–5 of the $x$ -coordinate represent the corresponding images in Figs. 9 (a–e), respectively.

as follow

$$\mathbf{H}^{(i+1)} = \arg\min_{\mathbf{H}} \left[ \alpha_3 \left\| \mathbf{U}^{(i)}\mathbf{H} - \mathbf{D} \right\|_2^2 + \beta_1 \left\| \mathbf{a}_1^{(i)} - \nabla\mathbf{H} - \mathbf{s}_1^{(i)} \right\|_2^2 \right] \tag{17}$$

When $\mathbf{H}$ holds for (18), the iterative process comes to an end

$$\alpha_3 \left(\mathbf{U}^{(i)}\right)^{\mathrm{T}} \left(\mathbf{U}^{(i)}\mathbf{H}^{(i+1)} - \mathbf{D}\right) - \beta_1 \Delta\mathbf{H}^{(i+1)} + \mathrm{div}\left(\mathbf{a}_1^{(i)} - \mathbf{s}_1^{(i)}\right) = \mathbf{0}. \tag{18}$$

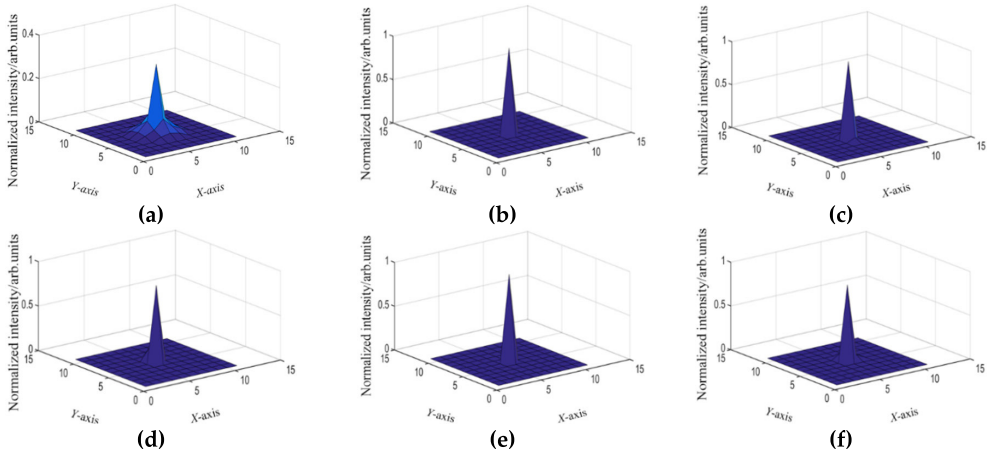


**FIGURE 12.** Polarization modulation imaging results of the PSF of a polystyrene sphere. (a) Non-optimized PSF, (b), (c) non-optimized PSF of the two polarization imaging results, (d) optimized PSF, and (e), (f) optimized PSF of the two polarization imaging results.

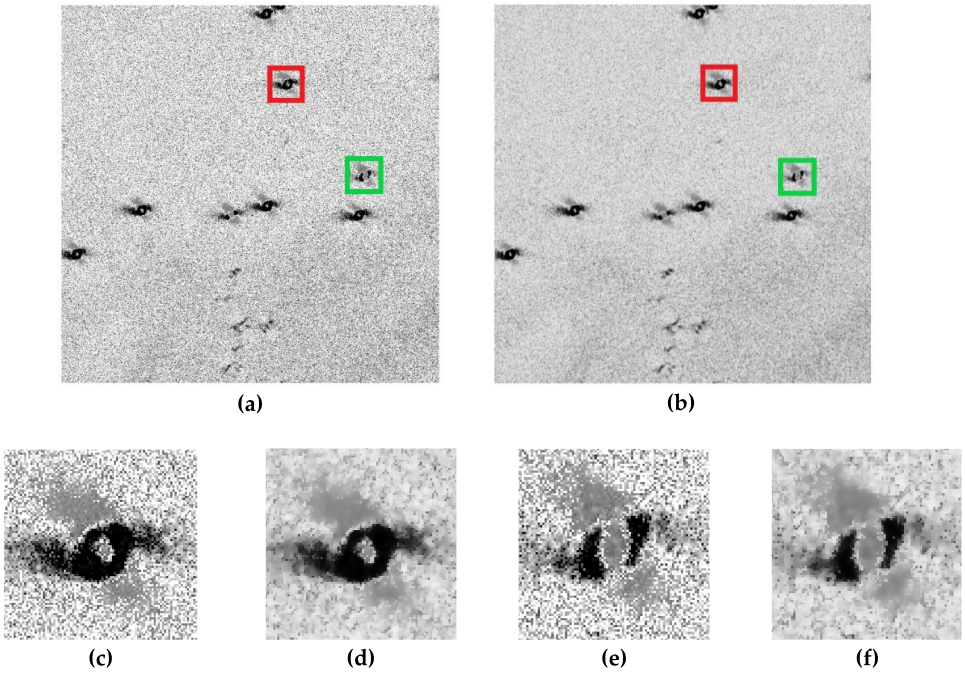


**FIGURE 13.** Results of the proposed method of one polarization image of the polystyrene sphere compared with the original image. (a), (c), (e) original and zoomed-in images, and (b), (d), (f) image obtained with the proposed method and zoomed-in images, where the red box represents the same position of (c) and (d), and the green box represents the same position of (e) and (f).

Then, we fix $\mathbf{H}^{(i+1)}$, $\mathbf{s}_1$, and $\mathbf{U}$, for sub-problem $\mathbf{a_1}$, which we can find via the variational principle as follow

$$\mathbf{a}_1^{(i+1)} = \arg\min_{\mathbf{a}_1} \left[ \alpha_1 \sum |\mathbf{a}_1|^{p(|\nabla \mathbf{T}|)} + \beta_1 \left\| \mathbf{a}_1 - \nabla \mathbf{H}^{(i+1)} - \mathbf{s}_1^{(i)} \right\|_2^2 \right]. \quad (19)$$

Sequentially, we can infer from the Euler–Lagrangian algorithm [33], [34] that

$$\alpha_1 p\left(|\nabla \mathbf{T}|\right) |\mathbf{a}_1|^{p(|\nabla \mathbf{T}|)-\frac{1}{2}} \mathbf{a}_1 + 2\beta_1 \left[ \mathbf{a}_1 - \nabla \mathbf{H}^{(i+1)} - \mathbf{s}_1^{(i)} \right] = \mathbf{0}. \quad (20)$$

Now, let $\mathbf{a}_1 = (\mathbf{a}_{11}, \mathbf{a}_{12})$ and $\mathbf{s}_1 = (\mathbf{s}_{11}, \mathbf{s}_{12})$. Then (20) can be transformed as follows

$$\begin{aligned} (c + 2\beta_1)\, \mathbf{a}_{11} - 2\beta_1 \mathbf{h}_x^{(i+1)} - 2\beta_1 \mathbf{s}_{11}^{(i)} &= 0 \\ (c + 2\beta_1)\, \mathbf{a}_{12} - 2\beta_1 \mathbf{h}_y^{(i+1)} - 2\beta_1 \mathbf{s}_{12}^{(i)} &= 0, \end{aligned} \quad (21)$$

where

$$c = \alpha_1 p\left(|\nabla \mathbf{T}|\right) \left(\mathbf{a}_{11}^2 + \mathbf{a}_{12}^2\right)^{\frac{p(|\nabla \mathbf{T}|)}{2}-1}. \quad (22)$$

A Newton method [35], [36] is used to optimize the solution in this paper. The relationship between $\mathbf{a}_{11}$ and $\mathbf{a}_{12}$ can

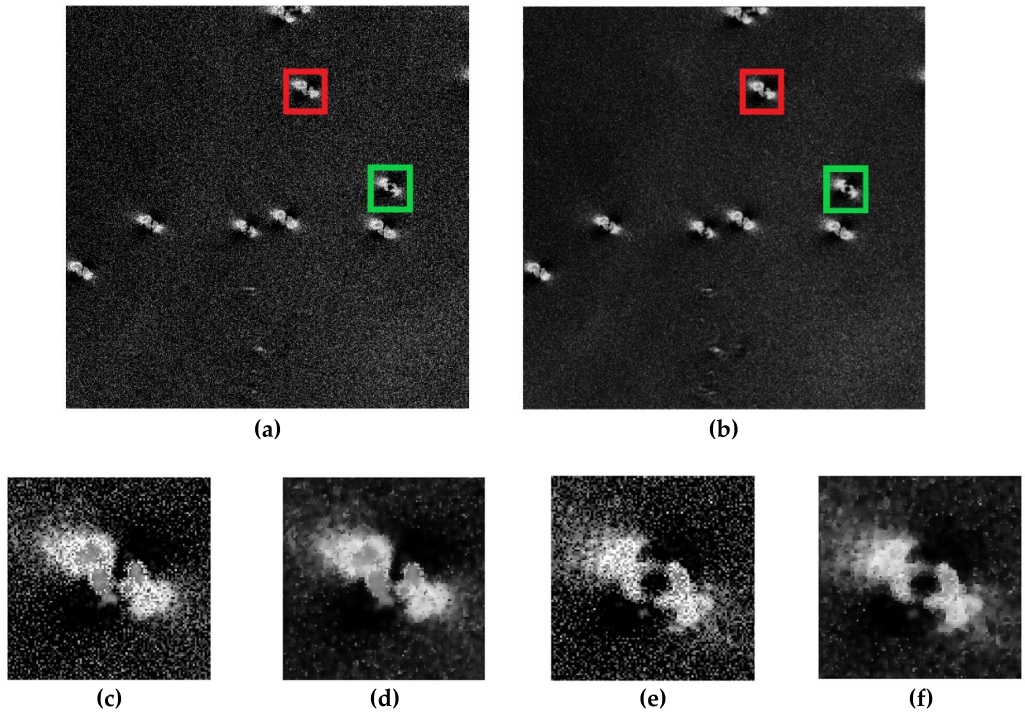


**FIGURE 14.** Results of the other polarization image of a polystyrene sphere obtained with our method compared with the original image. (a), (c), (e) Original and zoomed-in images, and (b), (d), (f) optimization results of the proposed method and zoomed-in images, where the red box represents the same position of (c) and (d), and the green box represents the same position of (e) and (f).

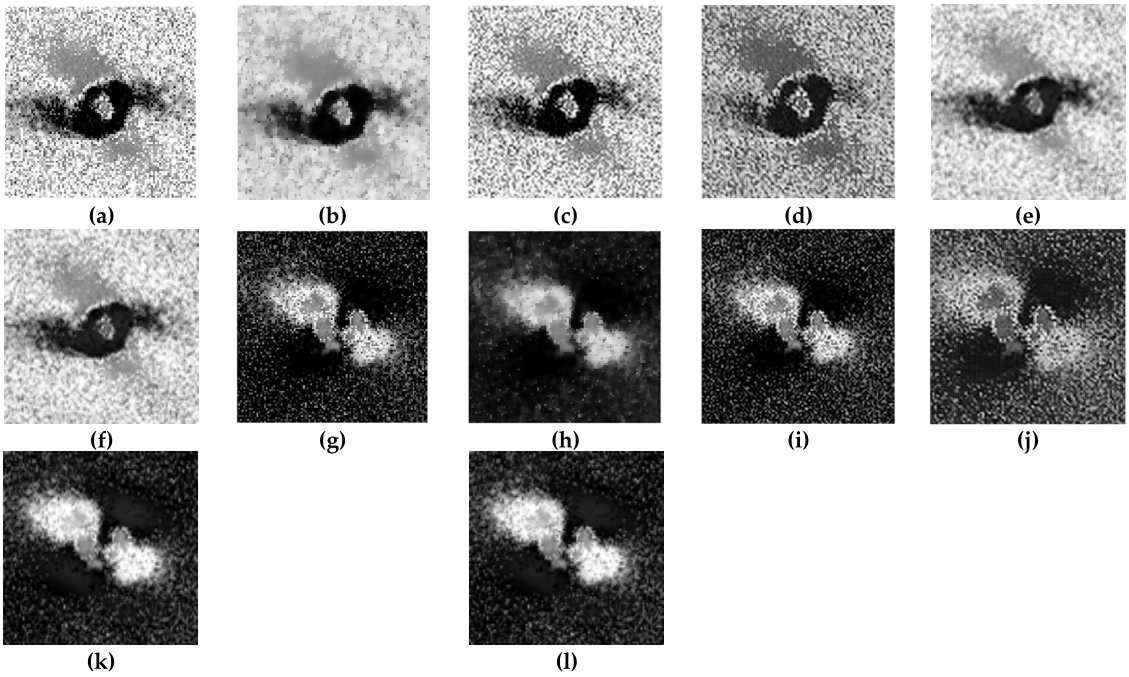


**FIGURE 15.** Comparison of imaging results of the polystyrene sphere obtained with the proposed method, Perrone's TV regularization, Lu's Tikhonov regularization, inverse filtering, and Wiener filtering. (a–f) Results of one polarization image, (g–l) results of the other polarization image. (a), (g) Original images, (b), (h) results of our method, (c), (i) results of Perrone's TV regularization, (d), (j) results of Lu's Tikhonov regularization, (e), (k) results of inverse filtering, and (f), (l) results of Wiener filtering.

be defined as follows

$$\mathbf{a}_{11} = \frac{\mathbf{h}_x^{(i+1)} + \mathbf{s}_{11}^{(i)}}{\mathbf{h}_y^{(i+1)} + \mathbf{s}_{12}^{(i)}} \mathbf{a}_{12}. \tag{23}$$

Then, we update $\mathbf{s_1}$ as

$$\mathbf{s}_1^{(i+1)} = \mathbf{s}_1^{(i)} + \nabla \mathbf{H}^{(i+1)} - \mathbf{a}_1^{(i+1)}. \tag{24}$$

**Algorithm 1** Variable Exponential Function Regularization

Input: The degraded image, $\mathbf{D}$;

Output: The reconstructed image, the real part of $\mathbf{D}'$;

1: Initial $R(\mathbf{H}) = \int |\nabla \mathbf{H}|^{p(|\nabla \mathbf{T}|)} \mathrm{d}\sigma$, where $p(m) = 1 + \frac{1}{1+nm^2}$, $\mathbf{H} = 0$, $\mathbf{T} = 0$, $m = 0$, $n = 0$, and $\mathbf{U} = 0$.

2: Set

$$\min_{\mathbf{H},\mathbf{U}} J(\mathbf{H}, \mathbf{U}) = \min_{\mathbf{H},\mathbf{U}} \begin{bmatrix} \alpha_3 \|\mathbf{H} \times \mathbf{U} - \mathbf{D}\|_2^2 + \alpha_1 R(\mathbf{H}) \\ +\ldots + \alpha_2 \int |\nabla \mathbf{U}| \, \mathrm{d}\sigma \end{bmatrix}$$

3: Iterate step 2 by Split-Bregman algorithm

4: Return $\mathbf{D}'$.

Finally, we fix $\mathbf{a}_1$, $\mathbf{s}_1$, and $\mathbf{H}$, and compute $\mathbf{a}_2$, $\mathbf{s}_2$, and $\mathbf{U}$.

After obtaining the PSF, a high-resolution image can be reconstructed according to a fast Fourier transform, which can be expressed as

$$\mathbf{D}' = \left\{ \mathcal{F}^{-1} \left[ \frac{\alpha_3}{\beta_2} \left( |\mathcal{F}(\mathbf{H})| \right)^2 \right] \right\}^{\left[ \frac{\alpha_3}{\beta_2} \left( \left| \overline{\mathcal{F}^{-1}(\mathbf{H})} \right| \right)^{\mathcal{F}(\mathbf{U})} - \mathcal{F}(\mathbf{H}) \right]}, \tag{25}$$

where the real part of $\mathbf{D}'$ is the reconstructed image.

Algorithm 1 and Algorithm 2 are pseudocodes of the proposed method and Split–Bregman algorithm, respectively.

## III. EXPERIMENTAL RESULTS AND ANALYSIS

### A. EXPERIMENTAL SETUP

The designed wide-field polarization modulation imaging system is shown in Fig. 4. A mercury lamp was used as the light source (LS). Linearly polarized light with an equidistant angle of 18 degrees was obtained using rotating polarized plates, which had an angle precision of 0.05 degrees at equal intervals. An objective lens was used as an optic, which had a magnification factor of 100 and a numerical aperture of 0.90. The specimens used in this paper are polystyrene nanoparticles and silicon nanoparticles, with a radii of 530 nm and 500 nm, respectively. Reflected light and backscattered light from the specimen were incorporated by the CCD (PiA2400-17gm, Basler) via an analyzer system composed of a quarter-wave plate (QWP) and an analyzer. Two images of the polarization parameters were obtained via the retrieval of the light-field information obtained by the CCD.

### B. RESULTS OF OVER- AND UNDER-RECONSTRUCTION

To explicitly describe the over- and under-reconstruction, we made a phase angle retrieval results of light field from polarization modulated imaging of the actual image of silicon sphere. Figure 5 shows a comparison of the proposed method and the over- and under-reconstruction. Figs. 5(a-d) represent the results of actual image, the proposed method, over-reconstruction, and under-reconstruction, where Figs. 5(e-h) are a single particle selected from the same red location of Figs. 5(a-d). As can be seen from Fig. 5, over-reconstruction retains a large amount of noise information, while

**Algorithm 2** Split-Bregman Algorithm

Input: The degraded image, $\mathbf{D}$;

Output: The optimal result, $\mathbf{D}'$;

1: Initial $\mathbf{H} = 0$, $\mathbf{U} = 0$, $\mathbf{a_1} = 0$, $\mathbf{a}_2 = 0$, $\mathbf{T} = 0$, $\mathbf{s}_1 = 0$, $\mathbf{s}_2 = 0$

1: Set

$$\begin{pmatrix} \mathbf{H}^{(i+1)}, \mathbf{U}^{(i+1)} \\ ,\ldots, \mathbf{a}_1^{(i+1)}, \mathbf{a}_2^{(i+1)} \end{pmatrix} = \underset{\mathbf{H},\mathbf{U},\mathbf{a}_1,\mathbf{a}_2}{\arg\min} \begin{bmatrix} \alpha_3 \|\mathbf{H}\mathbf{U} - \mathbf{D}\|_2^2 \\ +\ldots + \alpha_1 \sum |\mathbf{a}_1|^{p(|\nabla \mathbf{T}|)} \\ +\ldots + \alpha_2 \sum |\mathbf{a}_2| \\ +\ldots + \beta_1 \left\| \mathbf{a}_1 - \nabla \mathbf{H} - \mathbf{s}_1^{(i)} \right\|_2^2 \\ +\ldots + \beta_2 \left\| \mathbf{a}_2 - \nabla \mathbf{U} - \mathbf{s}_2^{(i)} \right\|_2^2 \end{bmatrix}$$

3: Fix $\mathbf{a_1}$, $\mathbf{s_1}$, and $\mathbf{U}$, compute

$$\mathbf{H}^{(i+1)} = \underset{\mathbf{H}}{\arg\min} \left[ \alpha_3 \left\| \mathbf{U}^{(i)}\mathbf{H} - \mathbf{D} \right\|_2^2 + \beta_1 \left\| \mathbf{a}_1^{(i)} - \nabla \mathbf{H} - \mathbf{s}_1^{(i)} \right\|_2^2 \right]$$

4: Until

$$\alpha_3 \left( \mathbf{U}^{(i)} \right)^{\mathrm{T}} \left( \mathbf{U}^{(i)}\mathbf{H}^{(i+1)} - \mathbf{D} \right) - \beta_1 \Delta \mathbf{H}^{(i+1)} + \mathrm{div} \left( \mathbf{a}_1^{(i)} - \mathbf{s}_1^{(i)} \right) = \mathbf{0}$$

5: Fix $\mathbf{H}^{(i+1)}$, $\mathbf{s}_1$, and $\mathbf{U}$, compute

$$\mathbf{a}_1^{(i+1)} = \underset{\mathbf{a}_1}{\arg\min} \left[ \alpha_1 \sum |\mathbf{a}_1|^{p(|\nabla \mathbf{T}|)} + \beta_1 \left\| \mathbf{a}_1 - \nabla \mathbf{H}^{(i+1)} - \mathbf{s}_1^{(i)} \right\|_2^2 \right]$$

6: Until

$$\alpha_1 p \left( |\nabla \mathbf{T}| \right) |\mathbf{a}_1|^{p(|\nabla \mathbf{T}|) - \frac{1}{2}} \mathbf{a}_1 + 2\beta_1 \left[ \mathbf{a}_1 - \nabla \mathbf{H}^{(i+1)} - \mathbf{s}_1^{(i)} \right] = \mathbf{0}$$

7: Update $\mathbf{s}_1$, compute

$$\mathbf{s}_1^{(i+1)} = \mathbf{s}_1^{(i)} + \nabla \mathbf{H}^{(i+1)} - \mathbf{a}_1^{(i+1)}$$

8: Fix $\mathbf{a}_1$, $\mathbf{s}_1$, and $\mathbf{H}$, compute $\mathbf{a}_2$, $\mathbf{s}_2$, and $\mathbf{U}$

9: Return $\mathbf{D}'$.

under-reconstruction smooths the particle boundary. The proposed method can sharpen the particle boundary while smoothing the noise information by proper reconstruction.

Figure 6 shows the light intensity profile corresponding to the position of the red line in Figs. 5(e-h). It can be seen that over-reconstruction sharpens the boundary of all the singular

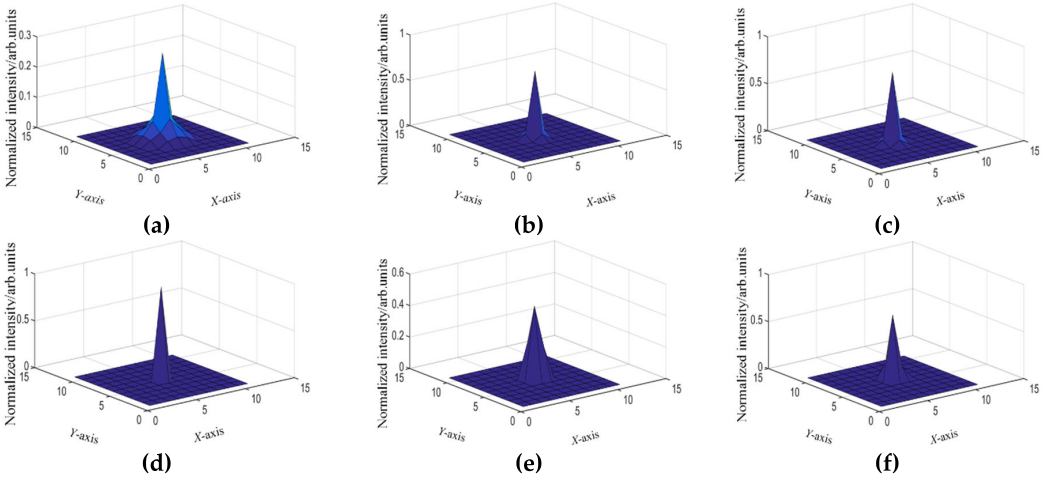


**FIGURE 16.** Polarization modulated imaging results of the PSF of a silicon sphere. (a) Non-optimized PSF, (b), (c) non-optimized PSF of the two polarization imaging results, (d) optimized PSF, and (e), (f) optimized PSF of the two polarization imaging results.

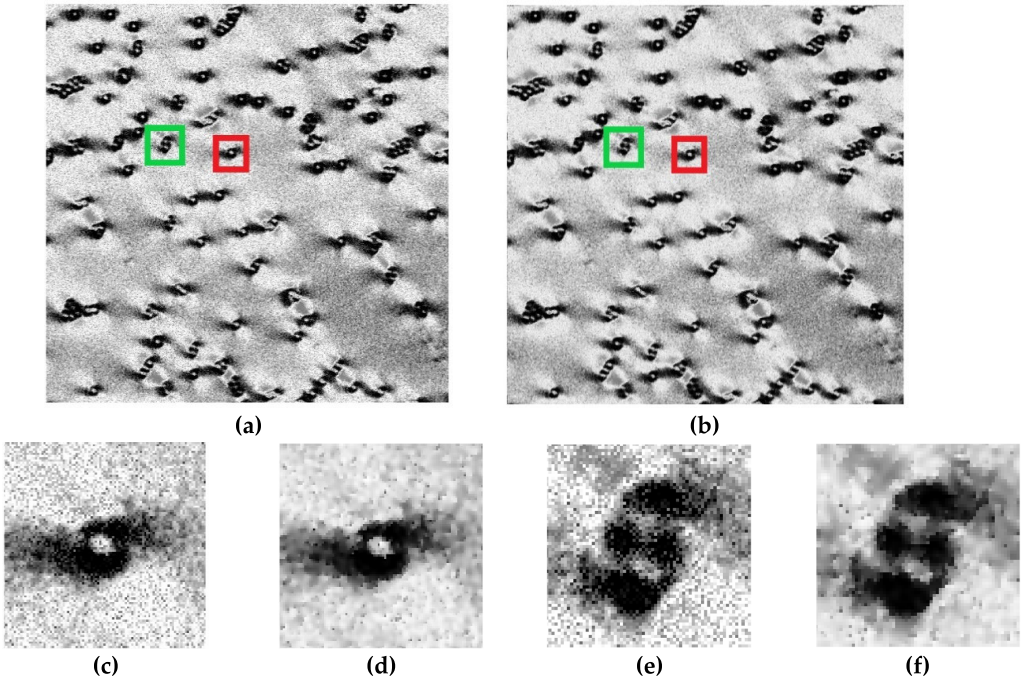


**FIGURE 17.** Results of the proposed method of one polarization image of the silicon sphere compared with the original image. (a), (c), (e) Original image and zoomed-in images, and (b), (d), (f) image obtained with the proposed method and zoomed-in images, where the red box represents the same position of (c) and (d), and the green box represents the same position of (e) and (f).

regions, while under-reconstruction smooths all the regions, which leads to a severe distortion of the reconstruction results. The proposed method can sharpen the particle boundary while smoothing the noise information.

### C. RESULTS OF THE FDTD SIMULATION

Generally, it is impossible to obtain a perfectly clear image of a specimen in actual systems. Instead an image generated by the FDTD simulation was degraded to verify the effectiveness of the proposed method. Figure 7 exhibits an original polarization image of the silicon sphere with a polarizer angle of 0 degrees without errors, where the simulated sphere has a radius of 50 nm, and the field-of-view is 1000 nm $\times$ 1000 nm. Figure 8 shows a comparison of the reconstructed results of the degraded image with different AGGD degradations and Poisson noise obtained with the proposed method, Perrone's TV regularization, Lu's Tikhonov regularization, inverse filtering, and Wiener

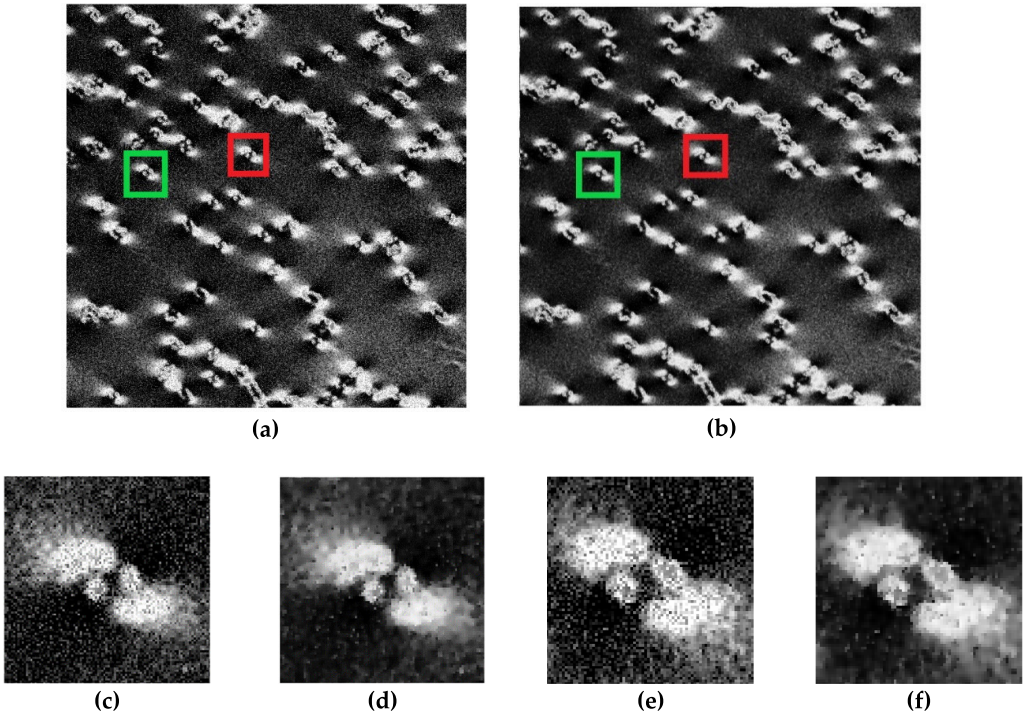


**FIGURE 18.** Results of the other polarization image of the silicon sphere obtained with our method compared with the original image. (a), (c), (e) Original image and zoomed-in images, and (b), (d), (f) the optimization results obtained with the proposed method and zoomed-in images, where the red box represents the same position of (c) and (d), and the green box represents the same position of (e) and (f).

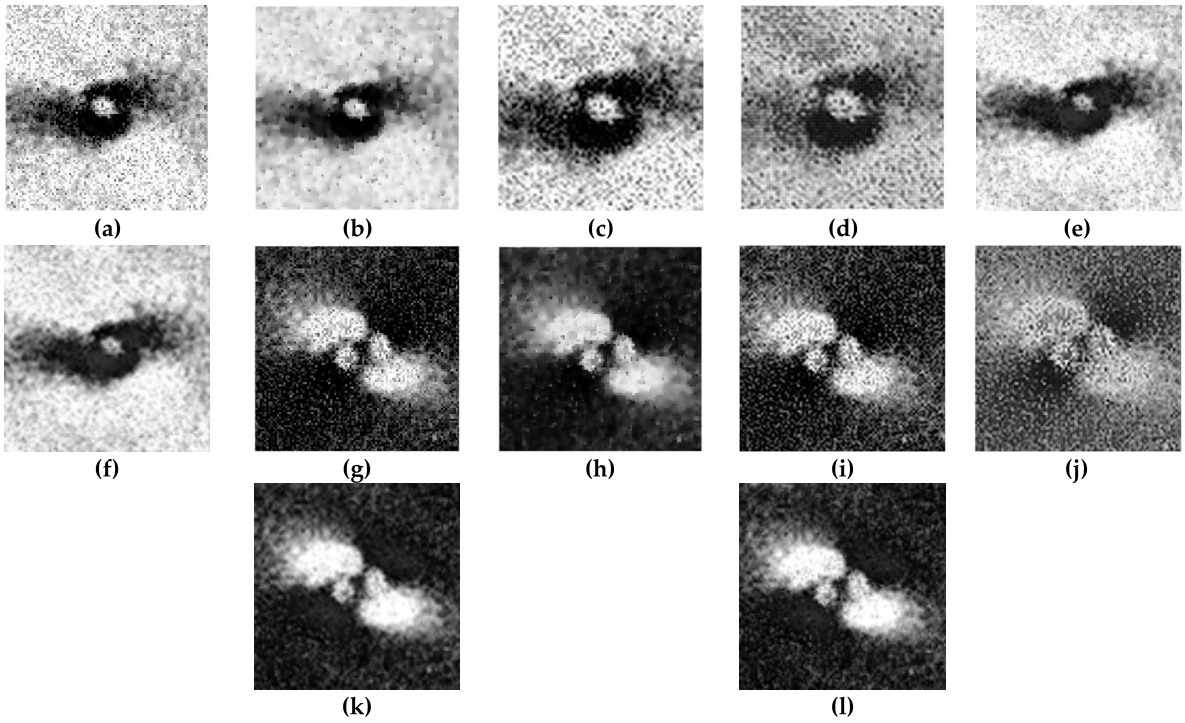


**FIGURE 19.** Comparison of reconstruction results of the silicon sphere obtained with the proposed method, Perrone's TV regularization, Lu's Tikhonov regularization, inverse filtering, and Wiener filtering. (a–f) Results of one polarization image, and (g–l) results of the other polarization image. (a), (g) Original images, (b), (h) results of our method, (c), (i) results of Perrone's TV regularization, (d), (j) results of Lu's Tikhonov regularization, (e), (k) results of inverse filtering, and (f), (l) results of Wiener filtering.

filtering. Perrone's TV regularization and Lu's Tikhonov regularization are representative methods, which have a good effect on image reconstruction. Fig. 8(a1) is a blurred image with AGGD degradation, whose shape parameter is 10 and the left and right variances are 3.21 and 38.4, respectively. In Fig. 8(b1), the shape parameter is 10 and the left and right

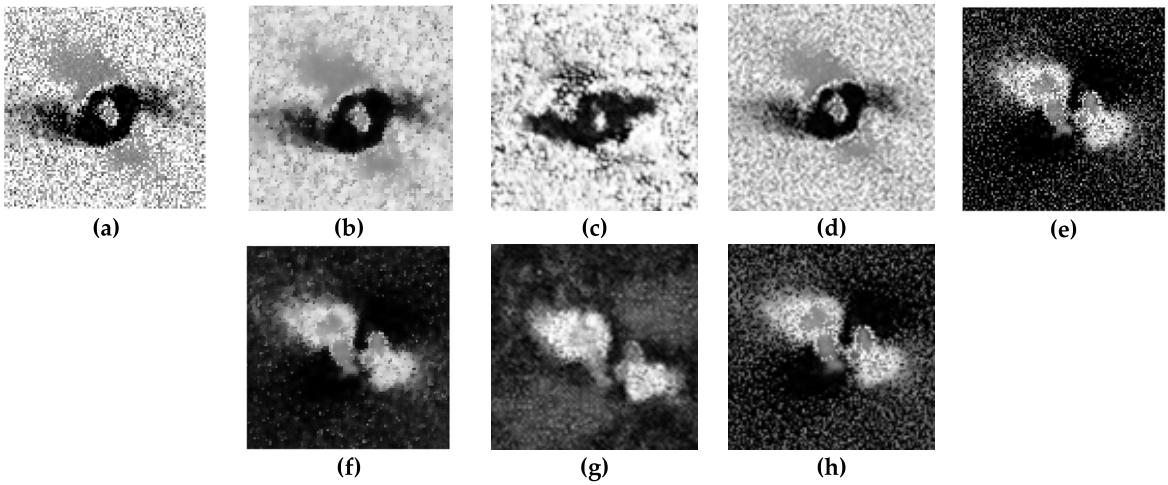


**FIGURE 20.** Comparison of imaging results of the polystyrene sphere obtained with the proposed method, DPPSR and DeblurGAN-v2. (a–d) Results of one polarization image, (e–h) results of the other polarization image. (a), (e) Original images, (b), (f) results of our method, (c), (g) results of DPPSR, and (d), (h) results of DeblurGAN-v2.

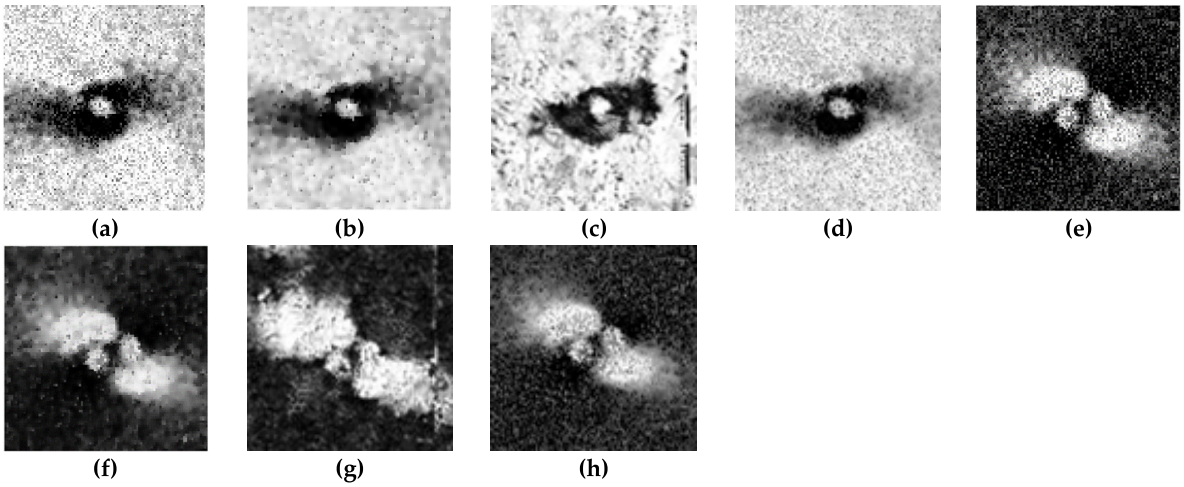


**FIGURE 21.** Comparison of imaging results of the silicon sphere obtained with the proposed method, DPPSR and DeblurGAN-v2. (a-d) Results of one polarization image, (e-h) results of the other polarization image. (a), (e) Original images, (b), (f) results of our method, (c), (g) results of DPPSR, and (d), (h) results of DeblurGAN-v2.

variances are 10.96 and 43.02, respectively. In Fig. 8(c1), the shape parameter is 10 and the left and right variances are 19.76 and 50.59, respectively. In Fig. 8(d1), the shape parameter is 5.62 and the left and right variances are 29.28 and 59.47, respectively. In Fig. 8(e1), the shape parameter is 3.36 and the left and right variances are 38.89 and 69.01, respectively. The parameter of additive Poisson noise is 10, 20, 30, 40, and 50 in Figs. 8(a1, b1, c1, d1, and e1), respectively. The mixed AGGD degradation is composed of AGGD degradation and Poisson noise.

From Fig. 8, we can infer that the proposed method is more effective in denoising than the comparison methods. It is more effective in dealing with mixed AGGD degradation with low variances. When the degradation is weak, images have less high-frequency information, and it is found that the methods compared here are all effective for image denoising and recovery. Nevertheless, when the degradation is gradually enhanced, high frequency information affects the calculation of the image gradient. Although the proposed method can also smooth the image in this case, the reconstructed image still contains some degradation.

Figure 9 presents objective assessment values of the images shown in Fig. 8. We chose some commonly used image quality assessment indices to quantify the differences of these methods, including the mean square error (MSE), peak signal-to-noise ratio (PSNR), structural similarity index measurement (SSIM), and the mean structural similarity index measurement (MSSIM). Here, 'Err' is the degraded image without processing, 'Inv' means inverse filtering, and 'Wien' represents Wiener filtering. 'Entropy' represents the degree of dispersion of the image information. The proposed method has advantages in almost all cases from Fig. 9, and

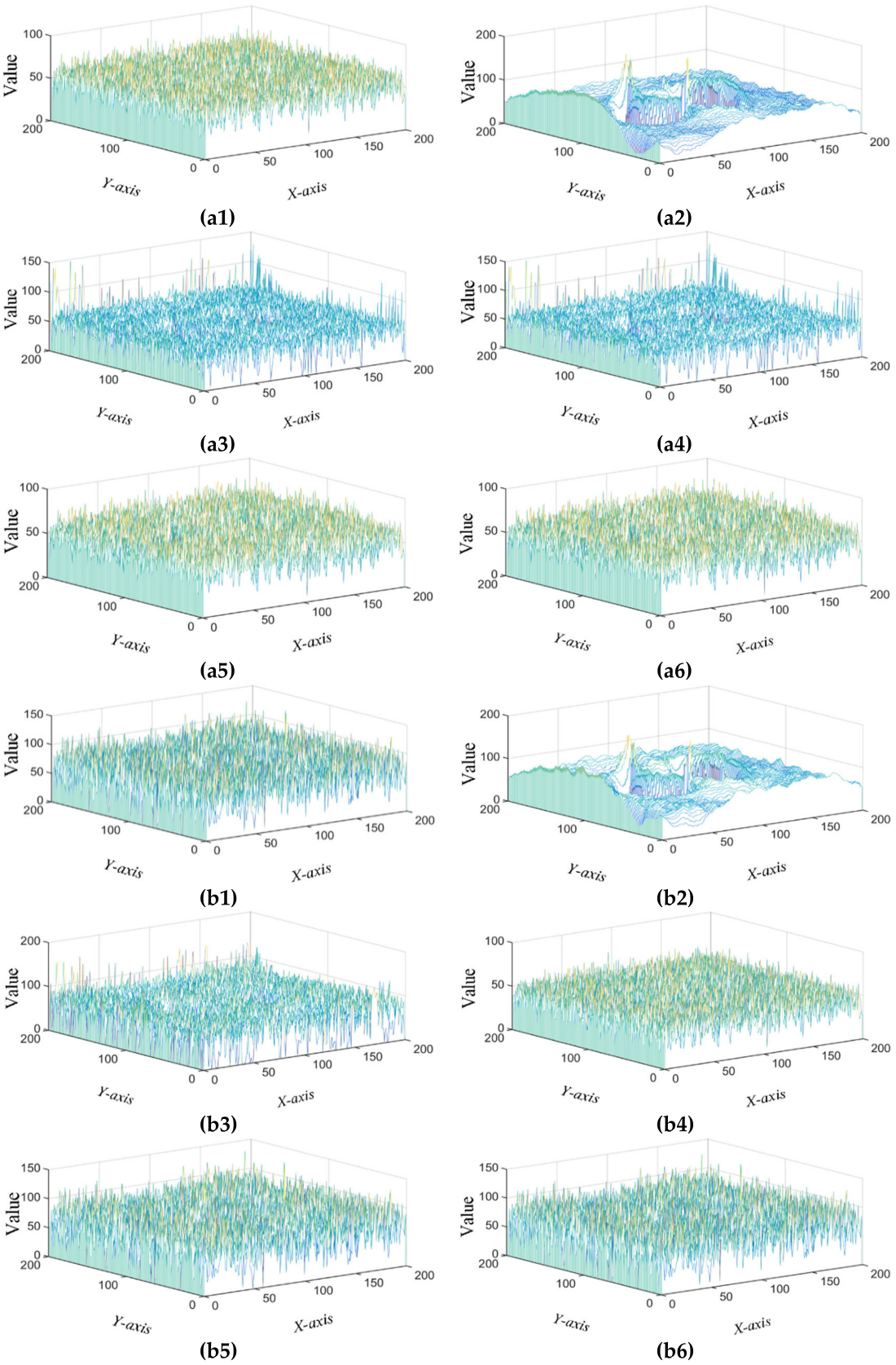


**FIGURE 22.** Waterfall diagrams of the difference between the comparison methods and the proposed method corresponding to Fig. 6. (a1, b1, c1, d1, and e1) show the degraded image without processing, and the reconstructed results obtained with (a2, b2, c2, d2, and e2) the proposed method, (a3, b3, c3, d3, and e3) Perrone's TV regularization, (a4, b4, c4, d4, and e4) Lu's Tikhonov regularization, (a5, b5, c5, d5, and e5) inverse filtering, and (a6, b6, c6, d6, and e6) Wiener filtering.

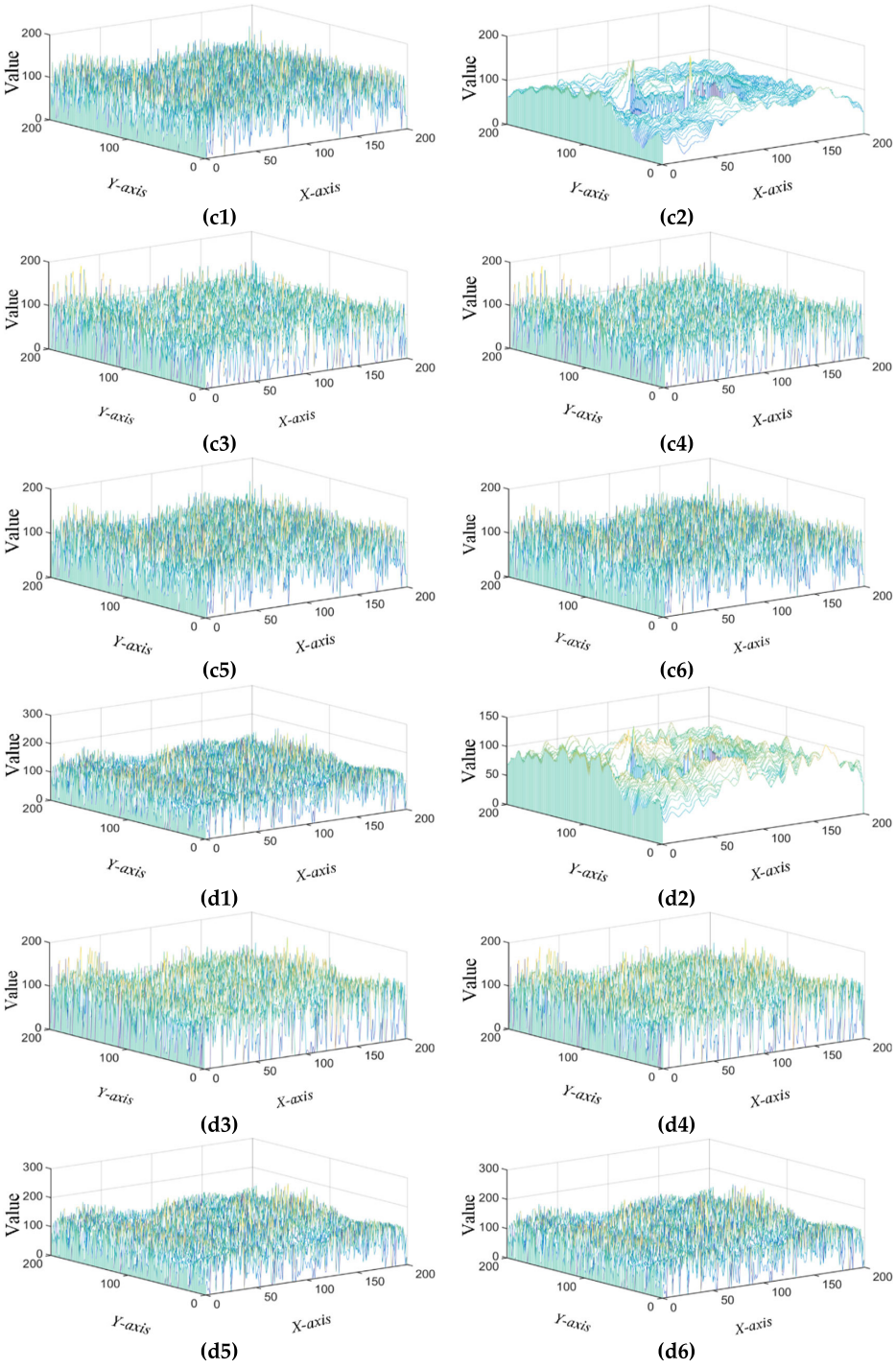


**FIGURE 22.** *(Continued)* **Waterfall diagrams of the difference between the comparison methods and the proposed method corresponding to Fig. 6. (a1, b1, c1, d1, and e1) show the degraded image without processing, and the reconstructed results obtained with (a2, b2, c2, d2, and e2) the proposed method, (a3, b3, c3, d3, and e3) Perrone's TV regularization, (a4, b4, c4, d4, and e4) Lu's Tikhonov regularization, (a5, b5, c5, d5, and e5) inverse filtering, and (a6, b6, c6, d6, and e6) Wiener filtering.**

is the most effective method in reducing image degeneration. The proposed method has highly ordered pixel distribution, as demonstrated by its denoising capability in terms of smoothing wings and sharpening edges, thereby resulting in low entropy.

We also compared our method with DPPSR [37] and DeblurGAN-v2 [38]. Since there is no qualified data set, we used the pre-training network to obtain the results directly. Figure 10 shows a comparison of the reconstructed results of the degraded image with different AGGD degradation

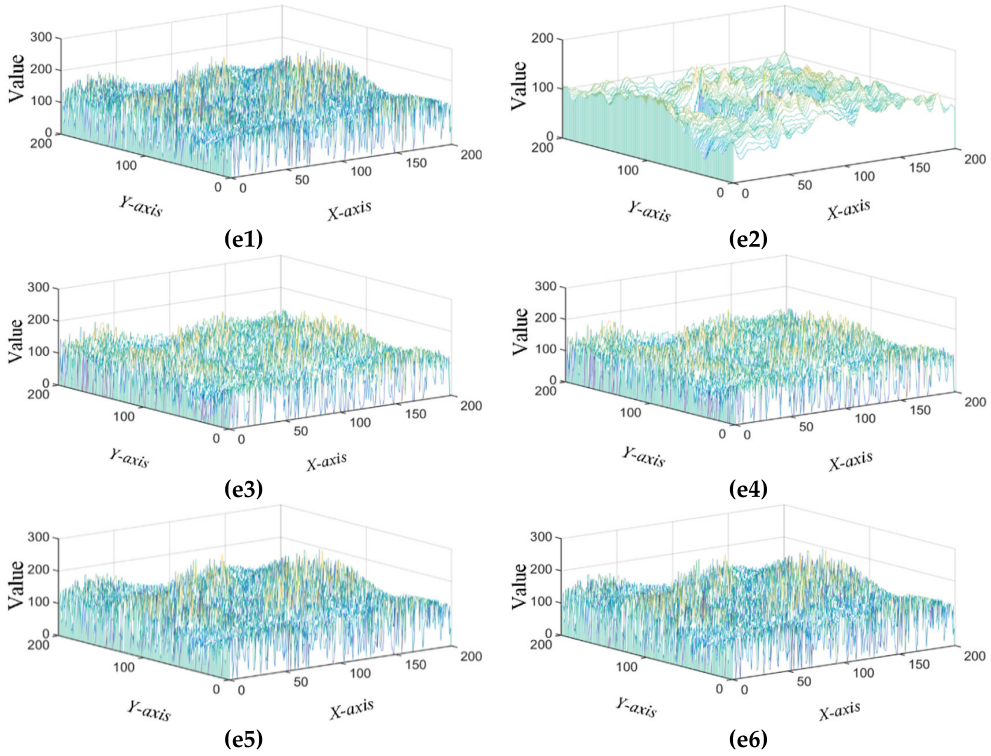


**FIGURE 22.** *(Continued)* **Waterfall diagrams of the difference between the comparison methods and the proposed method corresponding to Fig. 6. (a1, b1, c1, d1, and e1) show the degraded image without processing, and the reconstructed results obtained with (a2, b2, c2, d2, and e2) the proposed method, (a3, b3, c3, d3, and e3) Perrone's TV regularization, (a4, b4, c4, d4, and e4) Lu's Tikhonov regularization, (a5, b5, c5, d5, and e5) inverse filtering, and (a6, b6, c6, d6, and e6) Wiener filtering.**

values and Poisson noise obtained with the proposed method, DPPSR, and DeblurGAN-v2. Figure 11 shows the corresponding objective assessment values of the results in Fig. 10. From Figs. 10-11, compared with DPPSR and DeblurGAN-v2, the reconstructed result obtained with our method is superior. It is worth noting that when comparing different deep learning methods, due to the unknown parameters of the degradation model and the insufficient training set, it may be not possible to fit the network accurately.

See Appendix for more comparison.

### *D. RESULTS OF THE ESTIMATED POLARIZATION IMAGING PSF*

Figure 12 depicts a comparison of the PSF estimation results of the original image and the polarization parameter image obtained by the retrieval of light field of a polystyrene sphere. Fig. 12(a) presents the PSF model of the unprocessed image of the polystyrene sphere, while Figs. 12(b–c) display the PSF models of the two polarization imaging results, and Figs. 12(d-f) show the optimized PSF models obtained with the proposed method. A comparison between Figs. 12(a) and 12(d) illustrates that our method can adaptively reduce the amount of degradation in the PSF wings. Similarly, a comparison between Figs. 12(b–c) and 12(e–f) shows that our method can improve the image quality while ensuring retrieval accuracy.

We use the optimized estimation of the PSF of the polystyrene sphere presented in this paper to reconstruct the polarization imaging results, where Fig. 13 shows a result for one polarization image, and Fig. 14 depicts the result of another one. All the experimental figures, which present only one nanoparticle, have a size of $100 \times 100$ pixels, where a single pixel represents 34.5 nm. Compared with the original image, the resolution and image quality of the optimized image have been further improved. The reconstructed image obtained via the proposed method contains less degradation, has a smoother non-boundary particle region, and a sharper particle boundary region.

Next, Fig. 15 shows a comparison of imaging results obtained with our method, Perrone's TV regularization, Lu's Tikhonov regularization, inverse filtering, and Wiener filtering. From Fig. 15, it can be seen that compared with other methods, the imaging quality of ours is superior.

We also verified the results of our method using an image of a silicon sphere. Figure 16 shows a comparison of the PSF estimation results of an unprocessed image and polarization images. Further comparisons between the image reconstructed by the proposed method and the original image are shown in Figs. 17-19. It can be deduced from these images that the resolution and image quality of the optimized image have been further improved.

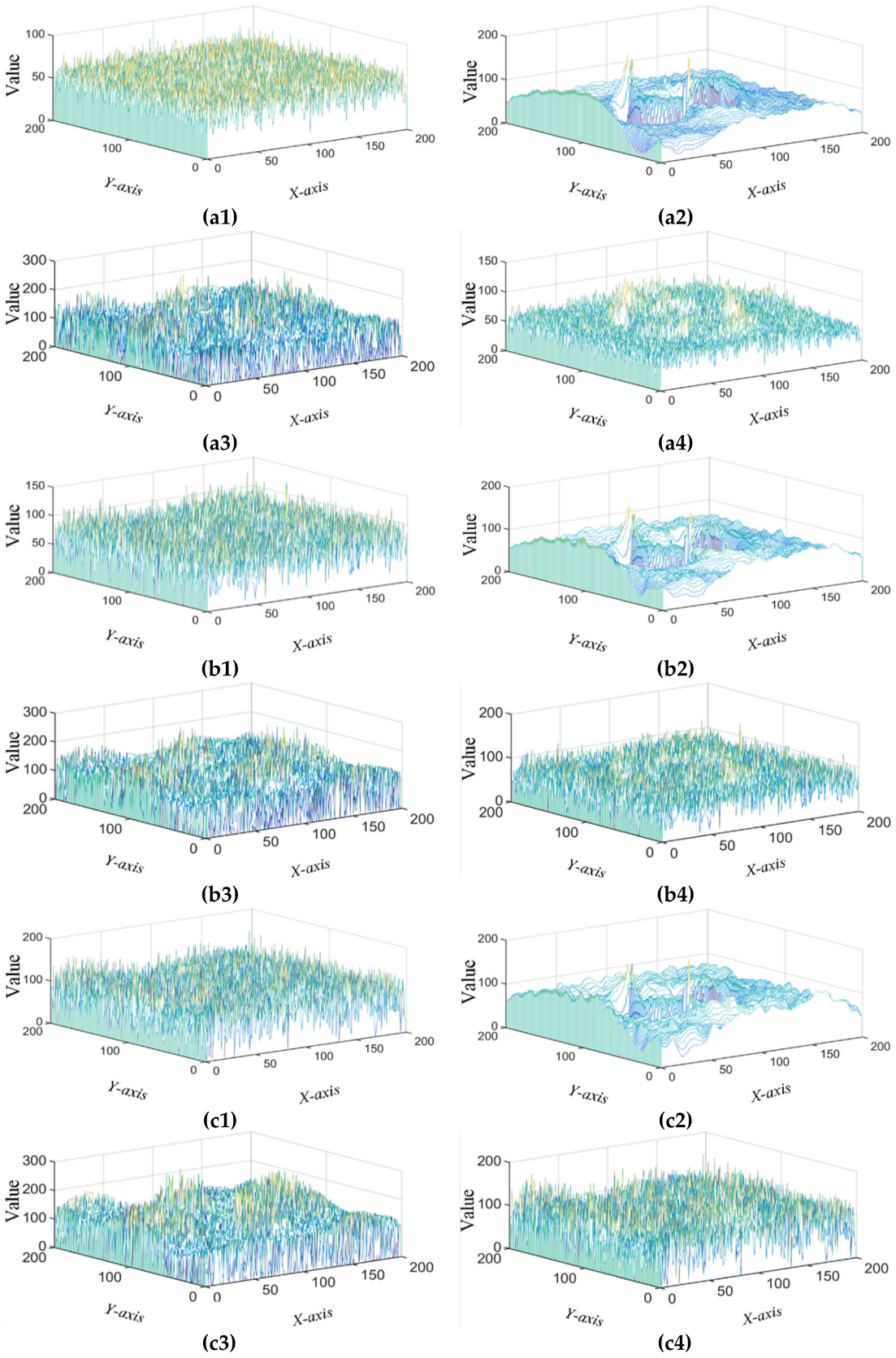


**FIGURE 23.** Waterfall diagrams of the differences between the comparison methods and the proposed method corresponding to Fig. 9. (a1, b1, c1, d1, and e1) show the degraded image without processing, and the reconstructed results obtained with (a2, b2, c2, d2, and e2) the proposed method, (a3, b3, c3, d3, and e3) DPPSR, and (a4, b4, c4, d4, and e4) DeblurGAN-v2.

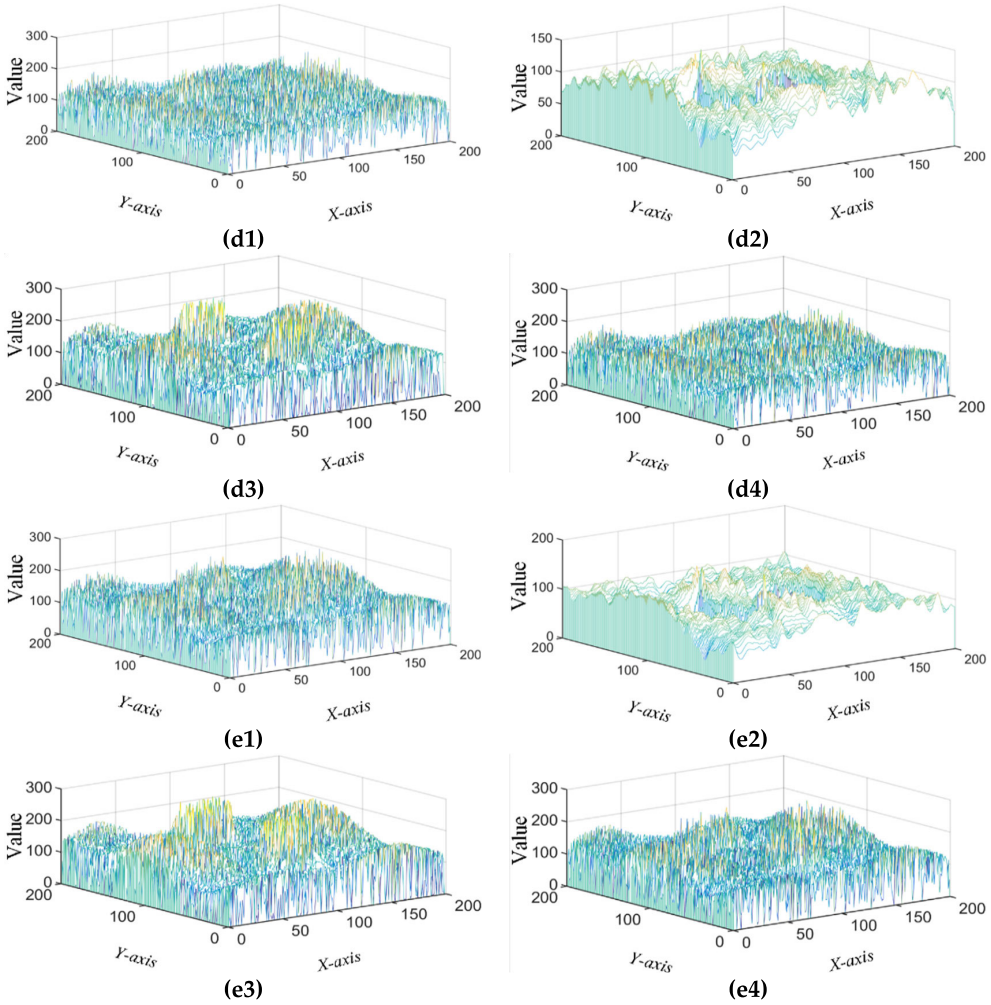


**FIGURE 23.** *(Continued)* **Waterfall diagrams of the differences between the comparison methods and the proposed method corresponding to Fig. 9. (a1, b1, c1, d1, and e1) show the degraded image without processing, and the reconstructed results obtained with (a2, b2, c2, d2, and e2) the proposed method, (a3, b3, c3, d3, and e3) DPPSR, and (a4, b4, c4, d4, and e4) DeblurGAN-v2.**

Finally, Figs. 20–21 show comparisons of the reconstructed results of the spheres obtained with the proposed method, DPPSR and DeblurGAN-v2. From Figs. 20–21, compared with DPPSR and DeblurGAN-v2, the reconstructed result of ours is superior.

## IV. CONCLUSION

In this paper, we proposed a novel method based on variable exponential function regularization to solve the lack of prior knowledge and the unknown parameters needed to estimate PSF degradation models. The main advantage of our method is that it can adaptively determine the norm according to AGGD degradation with uncertain parameters, which allows for a more flexible and effective approach to PSF estimation and reconstruction. Moreover, the proposed method can adaptively determine the norm according to image characteristics, thus effectively restraining the shortcomings of TV regularization and Tikhonov regularization. The results of actual specimens showed that, compared with traditional methods, the proposed method results in improvements of 18% in the PSNR, 21% in the SSIM, and 337% in the MSSIM. We are committed to balancing image accuracy and PSNR in the future.

## APPENDIX

To effectively describe the differences of the conventional methods with ours, we constructed the waterfall diagram shown in Fig. 22, which corresponds to the images shown in Fig. 6. It can be deduced that our method has the best performance in reducing global noise than the comparison approaches, particularly in the particle region.

Next, in Figs. 22 (a3, b3, c3, d3, and e3) and (a4, b4, c4, d4, and e4), the error matrices of Perrone's TV regularization and Lu's Tikhonov regularization have an approximate mean value of 100. From Fig. 9, the objective assessments of these two methods manifest as over-reconstruction and under-reconstruction. Inverse filtering and Wiener filtering had better results than TV regularization and Tikhonov regularization, as seen in Figs. 8, 9, and 22, but there exists an approximate mean value of 100 of global noise in Fig. 22.

The results indicate that although inverse filtering and Wiener filtering have better fitting effects than TV regularization and Tikhonov regularization, they are unable to accurately fit an AGGD. The mean global noise achieved with our method is below 100 and there are lower amounts of noise in the particle region. Indeed, in terms of the values of the objective indices, especially SSIM and MSSIM, our approach is superior to the other methods. Our method can limit the amount of over-reconstruction and under-reconstruction, and can better fit the AGGD.

In the same way, Fig. 23 shows that our method is superior to the comparative deep learning method.

## ACKNOWLEDGMENT

The authors would like to thank Gao Kun for discussions and critical reading of the manuscript. The authors are grateful to Zhao Hanwen and Xiong Jichuan, who provided the nanoparticle and retrieved images from their optical field information. The authors would also like to thank Li Mu, Zhang Zhenzhou, Hua Zizheng, Dou Zeyang, Wang Hong and Yu Peilin for useful discussions.

## REFERENCES

[1] Y. J. Liu, J. P. Xin, L. Y. Wan, and Z. H. Cai, "Optimization design of optical antenna with wide field-of-view high-gain subwavelength structure," *Laser Technol.*, vol. 41, no. 1, pp. 34–39, Jan. 2017.
[2] B. Q. Lao, A. N. Tao, X. Chen, X. C. Wu, and Y. Lu, "Research on wide-field imaging technologies for low-frequency radio array," *Acta Astronomica Sinica*, vol. 58, no. 5, pp. 110–131, Sep. 2017.
[3] P. Ma, J. Ni, J. Sun, X. Zhang, and J. Li, "Three-dimensional detection and quantification of defects in SiC by optical coherence tomography," *Appl Opt.*, vol. 59, no. 6, pp. 1746–1755, Jan. 2020.
[4] W. A. Iff, J. P. Hugomin, C. Sauvan, M. Besbes, and A. Bosseboeuf, "Electromagnetic analysis for optical coherence tomography based through silicon vias metrology," *Appl Opt.*, vol. 58, no. 27, pp. 7472–7488, Sep. 2019.
[5] X. Zhou, W. Sun, Z. Jiang, J. Ma, X. Zhang, Y. Byun, W. Chen, and J. Chen, "Modeling the CCD undersampling effect in the BATC photometric system," *Publications Astronomical Soc. Pacific*, vol. 117, no. 827, pp. 86–93, Jan. 2005.
[6] S. D. Zhong and L. Zheng, "Influence of CCD discrete pixels on the image quality," *Acta Metrol. Sinica*, vol. 19, no. 1, pp. 28–34, Jan. 1998.
[7] K. Ullah, X. Liu, M. Habib, and Z. Shen, "Subwavelength far field imaging of nanoparticles with parametric indirect microscopic imaging," *ACS Photon.*, vol. 5, no. 4, pp. 1388–1397, Jan. 2018.
[8] K. Ullah, X. Liu, N. P. Yadav, M. Habib, L. Song, and B. García-Cámara, "Light scattering by subwavelength $Cu_2O$ particles," *Nanotechnology*, vol. 28, no. 13, Feb. 2017, Art. no. 134002.
[9] Z. Lv, Y. Jia, and Q. Zhang, "Joint image registration and point spread function estimation for the super-resolution of satellite images," *Signal Process., Image Commun.*, vol. 58, pp. 199–211, Oct. 2017.
[10] H. Senshiki, S. Motohashi, T. Goto, H. Chen, and R. Aoki, "PSF estimation using total variation regularization and shock filter for blind deconvolution," in *Proc. IEEE Int. Conf. Consum. Electron. (ICCE)*, Las Vegas, NV, USA, Jan. 2017, pp. 460–461.
[11] K. M. Czajkowski, A. Pastuszczak, and R. Kotyński, "Real-time single-pixel video imaging with Fourier domain regularization," *Opt. Exp.*, vol. 26, no. 16, pp. 20009–20022, Apr. 2018.
[12] D. Perrone and P. Favaro, "A clearer picture of total variation blind deconvolution," *IEEE Trans. Pattern Anal. Mach. Intell.*, vol. 38, no. 6, pp. 1041–1055, Jun. 2016.
[13] G. Chen, G. Li, Y. Liu, X.-P. Zhang, and L. Zhang, "SAR image despeckling by combination of fractional-order total variation and nonlocal low rank regularization," in *Proc. IEEE Int. Conf. Image Process. (ICIP)*, Beijing, China, Sep. 2017, pp. 3210–3214.
[14] B. Du, Z. Huang, N. Wang, Y. Zhang, and X. Jia, "Joint weighted nuclear norm and total variation regularization for hyperspectral image denoising," *Int. J. Remote Sens.*, vol. 39, no. 2, pp. 334–355, Jan. 2018.
[15] J. Chen, X. Ju, E. Köbis, and Y.-C. Liou, "Tikhonov type regularization methods for inverse mixed variational inequalities," *Optimization*, vol. 69, no. 2, pp. 401–413, Feb. 2020.
[16] M. Zhai, G. Liu, Q. Tao, Z. Jiang, and M. Xin, "A novel approach for regularization matrix construction and its application in SBAS deformation model inversion," *Int. J. Remote Sens.*, vol. 41, no. 10, pp. 3708–3722, May 2020.
[17] X. Lu, L. Yang, M. Li, and X. W. Zhang, "Infrared and visible image fusion method based on Tikhonov regularization and detail reconstruction," *Acta Optica Sinic*, vol. 40, no. 2, Jan. 2020, Art. no. 0210001.
[18] Y. Rivenson, Y. Zhang, H. Gunaydin, T. Da, and A. Ozcan, "Phase recovery and holographic image reconstruction using deep learning in neural networks," *Light Sci. Appl.*, vol. 7, no. 2, May 2017, Art. no. 017141.
[19] J. Xu, L. Zhang, and D. Zhang, "A trilateral weighted sparse coding scheme for real-world image denoising," in *Proc. ECCV*, Munich, Germany, 2018, pp. 1–17.
[20] Z. S. Yue, Q. Zhao, L. Zhang, and D. Y. Meng, "Dual adversarial network: Toward real-world noise removal and noise generation," in *Proc. ECCV*, Glasgow, U.K., 2020, pp. 1–19.
[21] W. Cai and Z. Wei, "PiiGAN: Generative adversarial networks for pluralistic image inpainting," *IEEE Access*, vol. 8, pp. 48451–48463, Mar. 2020.
[22] M.-Y. Zou, *Deconvolution and Signal Recovery*. Beijing, China: National Defense Industry Press, 2001, pp. 189–194.
[23] Q. Wu, K. Gao, Z. Z. Hua, Z. Z. Zhang, H. W. Zhao, J. C. Xiong, and P. L. Yu, "Point spread function degradation model of a polarization imaging system for wide-field subwavelength nanoparticles," *Appl. Opt.*, vol. 59, no. 23, pp. 7114–7124, Aug. 2020.
[24] V. Zeljkovic, C. Tameze, D. J. Pochan, Y. Chen, and V. Valev, "Automated nanostructure microscopic image characterization and analysis," in *Proc. Int. Conf. High Perform. Comput. Simul. (HPCS)*, Amsterdam, The Netherlands, Jul. 2015, pp. 290–297.
[25] Y. Qian, J. Z. Huang, X. Li, and Y. Ding, "Robust nanoparticles detection from noisy background by fusing complementary image information," *IEEE Trans. Image Process.*, vol. 25, no. 12, pp. 5713–5726, Dec. 2016.
[26] K. Sentosun, I. Lobato, E. Bladt, Y. Zhang, W. J. Palenstijn, K. J. Batenburg, D. Van Dyck, and S. Bals, "Artifact reduction based on sinogram interpolation for the 3D reconstruction of nanoparticles using electron tomography," *Part. Part. Syst. Characterization*, vol. 34, no. 12, Oct. 2017, Art. no. 1700287.
[27] R. Machiraju and R. Yagel, "Reconstruction error characterization and control: A sampling theory approach," *IEEE Trans. Vis. Comput. Graphics*, vol. 2, no. 4, pp. 364–378, Dec. 1996.
[28] H. Lu, X. Li, L. Zhang, X. Ruan, and M.-H. Yang, "Dense and sparse reconstruction error based saliency descriptor," *IEEE Trans. Image Process.*, vol. 25, no. 4, pp. 1592–1603, Apr. 2016.
[29] K. Gao, Z. Zhu, Z. Dou, and L. Han, "Variable exponent regularization approach for blur kernel estimation of remote sensing image blind restoration," *IEEE Access*, vol. 6, pp. 4352–4374, Jan. 2018.
[30] S. Boyd, L. Vandenberghe, and L. Faybusovich, "Convex optimization," *IEEE Trans. Autom. Control*, vol. 51, no. 11, p. 1859, Nov. 2006.
[31] K. Xiong, G. Zhao, G. Shi, and Y. Wang, "A convex optimization algorithm for compressed sensing in a complex domain: The complex-valued split Bregman method," *Sensors*, vol. 19, no. 20, p. 4540, Oct. 2019.
[32] L. Chen, Z.-W. Zheng, L.-J. Bao, J.-S. Fang, T.-H. Yang, S.-H. Cai, and C.-B. Cai, "Weighted total variation using split Bregman fast quantitative susceptibility mapping reconstruction method," *Chin. Phys. B*, vol. 27, no. 8, Aug. 2018, Art. no. 088701.
[33] Y. Zhang, Z. Deng, and Y. Hong, "Distributed optimal coordination for multiple heterogeneous Euler–Lagrangian systems," *Automatica*, vol. 79, no. 12, pp. 207–213, May 2017.
[34] F. Flandoli and D. Luo, "Euler–Lagrangian approach to 3D stochastic Euler equations," *J. Geom. Mech.*, vol. 11, no. 2, pp. 153–165, Mar. 2019.
[35] G. Liang, S. Ren, S. Zhao, and F. Dong, "A Lagrange-Newton method for EIT/UT dual-modality image reconstruction," *Sensors*, vol. 19, no. 9, p. 1966, Apr. 2019.
[36] S. Huang, Z. Wu, and A. Misra, "A practical, robust and fast method for location localization in range-based systems," *Sensors*, vol. 17, no. 12, p. 2869, Dec. 2017.
[37] K. Zhang, W. M. Zuo, and L. Zhang, "Deep plug-and-play super-resolution for arbitrary blur kernels," in *Proc. IEEE/CVF Conf. Comput. Vis. Pattern Recognit. (CVPR)*, Long Beach, CA, USA, Jun. 2019, pp. 1671–1681.
[38] O. Kupyn, T. Martyniuk, J. Wu, and Z. Wang, "DeblurGAN-v2: Deblurring (orders-of-magnitude) faster and better," in *Proc. IEEE/CVF Int. Conf. Comput. Vis. (ICCV)*, Seoul, South Korea, Oct. 2019, pp. 8878–8887.

**QIONG WU** received the B.E. degree in communication engineering and the M.S. degree in electronic and communication engineering from Zhengzhou University, in 2012 and 2017, respectively. He is currently pursuing the Ph.D. degree with the Beijing Institute of Technology. His research interests include light inversion and image quality assessment.

**KUN GAO** received the B.A. degree in electrical engineering and the Ph.D. degree in instrument science and engineering from Zhejiang University, China, in 1995 and 2002, respectively. From 2002 to 2004, he was a Postdoctoral Fellow with Tsinghua University, Beijing, China. Since 2005, he has been with the Beijing Institute of Technology, Beijing, with a focus on infrared technology and real-time image processing. He is a member of the Optical Society of China.

**MU LI** received the Ph.D. degree in control science and engineering from the Beijing Institute of Technology, in 2015. He is currently working with AI Platform of Meituan-Dianping Group. His research interest includes image quality assessment.

**ZHENZHOU ZHANG** received the B.E. degree in optical engineering from the Beijing Institute of Technology, in 2018, where he is currently pursuing the master's degree in optical engineering with the School of Optoelectronics. His current research interests include deep learning and remote sensing image processing.

**ZIZHENG HUA** received the B.E. degree in electrical and information engineering from Southwest Jiaotong University, in 2015. He is currently pursuing the Ph.D. degree in optical engineering with the School of Optoelectronics, Beijing Institute of Technology. His current research interests include deep learning and image parallel processing based on multi-core parallel computing.

**HANWEN ZHAO** received the B.E. degree in materials engineering from the Jinling Institute of Technology, China, in 2017. He is currently pursuing the Ph.D. degree with the Nanjing University of Science and Technology. His research interests include image processing, machine learning, and deep learning.

**JICHUAN XIONG** received the B.E. degree in information engineering from Zhejiang University, China, in 2005, the M.S. degree in optical engineering from the Southwest Institute of Technical Physics, China, in 2008, and the Ph.D. degree in physics from the University of Leuven (KU Leuven), Belgium, in 2013. He is currently with the Nanjing University of Science and Technology. His research interests include super-resolution imaging and photoacoustic imaging.

**ZEYANG DOU** received the B.E. degree in mathematics from Baoding University, China, in 2012, and the M.S. degree in computational mathematics from the Communication University of China, Beijing, China, in 2016. He is currently pursuing the Ph.D. degree with the Beijing Institute of Technology. His research interests include image processing, machine learning, and deep learning.

**HONG WANG** is currently pursuing the Ph.D. degree with the College of Optics and Photonics, Beijing Institute of Technology, Beijing. Her research interests include remote sensing image scene classification, semantic segmentation, pattern recognition, and machine learning.

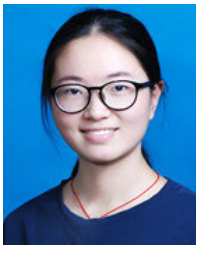

**PEILIN YU** is currently pursuing the bachelor's degree in computer science and technology with the Beijing Institute of Technology. Her research interests include image processing and big data analytics.